12-21-2020

Characterization of Ti-6Al-4V Cellular Structures for Bone Scaffolds Application

Muhammad Abdus Salam

CHARACTERIZATION OF TI-6AL-4V CELLULAR STRUCTURES FOR BONE SCAFFOLDS APPLICATION FABRICATED BY LASER-BASED POWDER-BED FUSION

By

Muhammad Abdus Salam

A Thesis

Submitted in Partial Fulfillment of the

Requirements for the Degree of

Master of Science

Major: Mechanical Engineering

The University of Memphis

December 2020

ACKNOWLEDGEMENTS

I would like to thank Dr. Ebrahim Asadi not only for providing me the opportunity to carry out this study but also for his guidance throughout the study.

I would like to extend my thankfulness to the committee members (Dr. Gladius Lewis, Dr. Gary Bowlin, Dr. Amir Hadadzadeh) for their valuable suggestions and time.

My gratitude to the lab members of the MAMLAB at the University of Memphis.

ABSTRACT

Additively manufactured Ti-6Al-4V cellular structures are the most popular metallic choices for bone tissue engineering (BTE) applications. In this work, laser-based powder bed fusion (PBF) technology was employed to fabricate Ti-6Al-4V cellular structures with geometries mimicking human cancellous bone properties. This study introduces novel laser scanning strategies with their associated laser-based PBF processing parameters for the fabrication of fine resolution Ti-6Al-4V cellular structures with tailored mechanical properties to improve their mechanical performance. Two distinct designed geometries, diamond and dodecahedron, in four different pore sizes were manufactured by employing three different laser-based PBF scanning strategies in combination with various laser power and scanning speeds while the laser spot size (~80μm), average powder size (34μm), and layer thickness (30μm) remained unchanged throughout the study. The observed finest resolution of struts for the manufactured cellular structures was 120μm. Later, correlations between laser-based PBF processing parameters/scanning strategies and physical/mechanical properties were investigated in this study. The properties of several fabricated dodecahedron structures demonstrated the ability to mimic human cancellous bone properties by exhibiting compressive strength, modulus of elasticity, and porosity in the range of 0.1-30MPa, 0.01-3GPa, and 72.6-87.4%, respectively. The concluding remarks on conceivable propriety for BTE applications incorporated the sets of scanning strategies and particular unit cell sizes of dodecahedron cellular structure.

TABLE OF CONTENTS

TABLE OF CONTENTS (CONTINUED)

LIST OF TABLES

LIST OF TABLES (CONTINUED)

LIST OF FIGURES

LIST OF FIGURES (CONTINUED)

CHAPTER 1

INTRODUCTION

1.1 Overview

This chapter discusses the background which is required to perform this thesis study on Ti-6Al-4V cellular structures for bone scaffold applications made by laser-based powder bed fusion (PBF) technology. The background includes the relative picture of bone defect in the USA, bone biology, bone replacement methods and materials, and scaffolds fabrication techniques. Later, elaborate discussion on direct metal laser sintering (DMLS), one of the most used laser-based PBF technology, processing parameters added as this study is focused on exploring DMLS scanning strategies.

1.2 Bone Defect

The bone defect is one of the major problems for human society. After the surgical procedure for the removal of a bone infection or bone tumors or non-union of bones after fracture may lead to having defects in bones. This can be not only a health hazard for the patient but also an economic burden. Every year within the United States, bone defect repairing treatment cost is more than $2.5 billion bringing about in excess of 2 million bone repair procedures, approximately [1,2].

1.3 Bone Biology

Successful bone repair treatments depend on the understanding of bone physiology. Based on the structural tissues, bones are classified into two types: 1. Cancellous bone and 2. Cortical bone, illustrated in Figure . Highly vascularized (>60% porosity) inner, softer part of the bone is made of cancellous tissues. Compressive strength and elastic modulus are relatively low for Cancellous tissues and in the range of 0.1-30MPa and 0.01-3GPa, respectively. On the other hand, cortical tissues form the outermost and denser boundary of the bone. Compressive strength and elastic modulus for the harder and denser (~5% porosity) cortical tissues are in the range of 130-225MPa and 3-30GPa, respectively. Bone is constituted of about 70% hydroxyapatite (HA) crystals and about 30% of water, collagen proteins, proteoglycans mixture [3].

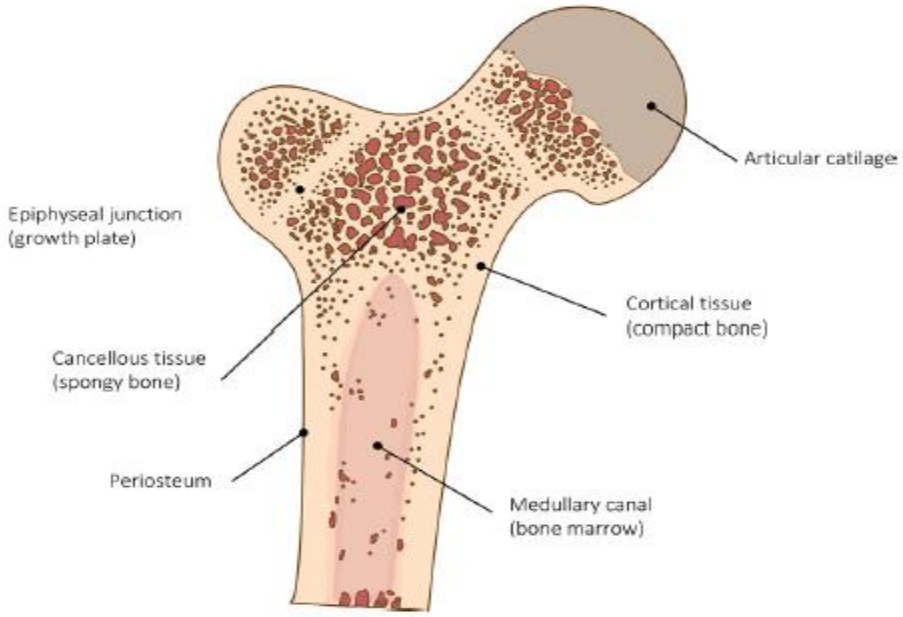

Figure 1: Schematic diagram of bone tissue [3].

1.4 Bone Grafts

Natural fracture healing process can't maintain and restore the integrity of bone when there is an excessive damage or defect. In this event, external intervention is required to provide the mechanical support and/or the initiation of bone regeneration process. To this day, clinicians rely on bone substitute materials for bone repair and regeneration procedures. Autografts and allografts are widely used bone substitute materials for clinical treatment of bone repair. Autografts, performed by autologous transplantation, are classified as the gold standard for bone grafts. Histocompatibility and non-immunogenicity are two very important characteristics of autografts but containing the essential properties for new bone growth such as osteoconductivity, osteogenicity and osteoinductivity elevated autograft as the ideal bone graft. Osteo-conductivity allows the attachment of new osteoblasts (cells that synthesize bone) and osteoprogenitor cells while facilitating the cell migration and vessel formation by maintaining the interconnected structure. Osteogenecity refers to the quality of bone grafts that supports bone growth while co-existing with pre-existing bone. Osteo-inductivity permits the differentiation of stem cells into osteoblasts. However, the secondary injury occurred due to the second operation for harvesting the

autografts from the iliac crest/distal femur/proximal tibia may lead to significant complications for the donor site. Other drawbacks of autografts are donor site morbidity, limited harvesting options as well as costly. On the other hand, allografts rely on donor bone tissue transplantation. It prevents the complications from the second operation, but risks of immunoreactions and disease transmission are very high [4,5].

1.5 Bone Tissue Engineering

The field of Bone Tissue Engineering (BTE) emerges as an alternative treatment option to those bone grafts with a goal to overcome the drawbacks encountered by bone grafts. In other words, BTE will possess all ideal characteristics (highly osteoinductive and angiogenic, low morbidity, readily available etc.) to facilitate bone repair. BTE refers to the intricate dynamic process which facilitates the proliferation, differentiation of osteoprogenitor cells, and eventually, leads to the matrix formation along with remodeling of the bone. Biocompatible scaffolds, growth factors, gene and drug deliveries are key factors for the advancement of BTE [4,6].

1.6 Scaffolds

Scaffolds are mechanical structures inserted to the defect site to provide mechanical support while repairing and regeneration of bone. The goals of scaffolds are creating an environment to initiate and facilitate the bone remodeling process with minimal complications. The processes to be followed are adherence of MSCs to the surface of scaffolds and formation of bone. To allow these processes go smoothly, scaffolds should possess some important characteristics.

i. Biocompatibility: The first and foremost characteristic of a scaffold is biocompatibility. A scaffold should not import toxicity to the host injury site. On the other hand, it must support cellular activity. Scaffold must promote bone cell adherence, proliferation, and formation of the extracellular matrix. Supporting the recruitment of progenitor cells and induction of bone formation through biomolecular signaling should be the characteristics of a scaffold. Moreover, angiogenesis should be facilitated by the scaffold to maintain nutrients, oxygen, and waste transportation [7].
ii. Mechanical Properties: An ideal scaffold should perfectly match the mechanical properties of bone. This is required to avoid the stress shielding effect. Compressive strength and elastic modulus for Cancellous tissues are in the range of 0.1-30MPa and 0.01-3GPa,

respectively. Compressive strength and elastic modulus for cortical tissues are in the range of 130-225MPa and 3-30GPa [3].

iii. Pore Size and Porosity: Interconnected porosity is an important feature of scaffolds. Interconnecting pores support the supply of nutrients and oxygen and transportation of metabolic waste as well. These are extremely important for the survival of cells. These pores also serve as routes for blood vessels. Cell attachment, biodegradation, and drug release rates are directly related to porosity as porosity determines the surface area available for the cell-scaffold interaction. However, excessive porosity weakens the scaffold structure mechanically. This implies the optimization of pore sizes. The optimum sizes of pores for effective bone growth are in the range of 200-350μm [8].

iv. Surface Morphology: Surface morphology directly affects the success rate of a scaffold because the primary cell attachment depends on appropriate surface roughness [3].

v. Bioresorbability: Bioresorbability refers to the degradation of scaffolds with time preferably at a controlled resorption rate. This resorption of scaffolds will free up space for new tissue to grow. The rate of resorption should match with the rate of tissue growth. In addition to that, the resorption of scaffolds must not bring toxicity to the site, related with the biocompatibility. Metabolization and elimination of degraded products from the body is also expected [7,9].

vi. Surface Permeability: Surface permeability is another notable feature of a scaffold. Surface permeability controls the transportation of biological fluid at the boundary. This impacts bone growth significantly. However, it reduces the mechanical strength of the scaffold [3,10].

1.7 Scaffolds Materials

Metals, ceramics, and natural or synthetic polymers are used for the fabrication of bone scaffolds. However, weak mechanical properties of ceramics and polymer scaffolds made the metallic scaffolds preferable over those [11,12].

Metals are the oldest and most widely used bone replacement materials. The use of metals for bone defect treatment started with implants and in recent decades, concentrated in scaffolds. Biocompatible, non-toxic, and corrosion-resistant titanium (Ti) and tantalum (Ta) alloys are used

frequently for dental and orthopedic applications. However, these metals are not biodegradable. Moreover, there are concerns over releasing metal ions. Exploration of magnesium (Mg) and its alloys is in the early stages for BTE applications. Bio-resorbabililty, high biodegradability, suitable mechanical properties, non-inflammatory responses are the main characteristics of scaffolds made of Mg [6,13].

Composite metal scaffolds can achieve the biodegradability, a lacking for metallic scaffolds. Magnesium alloys are leading in this purpose. Mg-Ca-Sr ternary alloy improves cell adhesion and degradation rates. Nickel-based and titanium-based 3D porous scaffolds with sodium hydroxide enhance cell attachment and proliferation [13,14].

1.8 Scaffolds Fabrication Techniques

Successful fabrication of functional scaffolds should pay attention closely in two levels: 1) microscale level should create an environment suitable for cell survival, 2) macroscale construction should promote cellular activities while possessing the required mechanical properties. Two widely used scaffolds fabrication techniques are conventional and rapid prototyping (RP) methods. Controlling microscale and macroscale features is very difficult in convention techniques. On the other hand, RP techniques not only allow the independent control of macroscale and microscale features but also support massive tissue formation through 3D bed fabrication and offer opportunities for manufacturing customized scaffolds combined with clinical imaging data and fabrication techniques. Powder bed fusion (PBF) 3D fabrication techniques have emerged as the popular techniques for scaffolds fabrication [15].

1.9 Powder Bed Fusion (PBF)

Selective laser melting (SLM) and Selective laser sintering (SLS) are the most common types of laser-based powder bed fusion (PBF) technologies. The difference between SLM and SLS is as simple as SLM completely melts the powder whereas SLS just fuses the powder without reaching the melting point. However, the general process is the same and relatively straightforward for both of the cases. The beginning of the process starts as a powder media which is stored in a dispenser reservoir. The reservoir dispenses a given amount of media made available to the recoat spreader, which depending on the type of machine, could be a hard scraper, soft squeegee, or roller. This media is dispensed on a build plate and a selective portion in selective positions of the media are

sintered/fused by a focused laser moving across the surface. These lasers are typically fiber lasers with wavelengths in the 1.06-1.08-µm range and powers on the order of magnitude of 100 W. After the laser sintered/fused the media, the build plate lowers, and a new layer of media is applied, repeating the whole process eventually creating a finished part. When the SLS process is applied to the metal alloys, then it is referred as Direct Metal Laser Sintering (DMLS). For metals, the process is generally taken place in a nitrogen or argon atmosphere with a very low oxygen content to prevent oxidation of the metal during the fusion process. Figure 2 shows the typical operation and components of the SLS process [16].

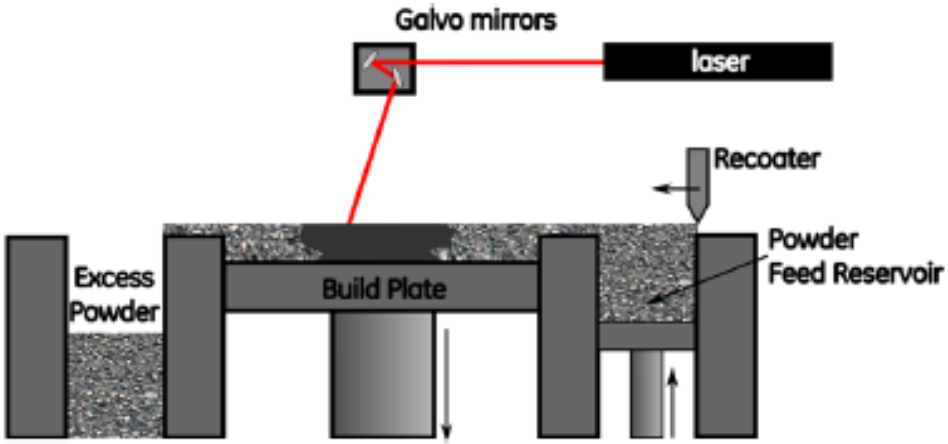

Figure 2: The typical operation and components of the SLS process [16].

There are advantages as well as drawbacks of the SLS process. The ability to create objects with complex geometry and internal features is a major advantage. This creates the way of controlling pore size and porosity independently. Another advantage is the large selection of biomaterials available. SLS currently supports most biomaterials such as polymers, ceramics, nickel, and titanium. There are different types of drawbacks to this process. There are space constraints such as a large amount of room required to store the equipment and the machines require a relatively large amount of power for operation. Another drawback is possible part defects that are caused by the build process. These defects can be major structural flaws that negatively impact mechanical properties such as delaminating or cracking which is common in the SLS process. Delamination is the cracking or separation of build layers which can be caused by improper heating or cooling of the part, leading to warping, during the building process or by oxidation forming on the build surface between layers. Another type of structural defect is residual stresses, also very common

for SLS, due to grain structure and are caused by large thermal gradients throughout the production [17].

Electron beam melting (EBM) is another PBF technology, which also follows the layer-by-layer methods. EBM uses an electron beam to melt/fuse the powder rather than using laser power, this indicates the difference, the most significant one, between laser-based PBF and EBM. In addition to that, the build environment is extremely hot in comparison with laser-based PBF. Overnight cooling of build plate is mandatory for the next run after the completion of a job. Unlike the laser-based PBF, which runs under an inert atmosphere, the EBM process runs under a vacuum atmosphere [18].

Processing brittle materials without the formation of solidification cracks are the major advantage of the EBM process. Laser-based PBF technology employs very high cooling rates from their melting points/solidifying ranges, resulting the formation of solidification cracks. EBM process avoids the solidification cracks by applying very slow cooling rates. Moreover, oxidation is generally averted due to the vacuum chamber. However, very limited materials can be employed in EBM (Ti grade 2, Ti-6Al-4V, Inconel 718, CoCrMo) as the optimization of processing parameters is difficult. Alloys that contain volatile constituents such as Zn, Mg, Pb, Bi, etc. should be avoided due to the very high build temperatures. In addition to that, this slow process makes the parts expensive [18].

1.10 DMLS Process Variables

In the aspect of key process variables of PBF technology, there are many parameters that directly impact the quality of the finished product. The primary parameters consist of laser and scanning, powder material properties, powder bed properties and recoat, and the build environment. Unfortunately, not all of these parameters are controllable. One major variable the user has control over is the laser behavior, including the power level of the laser, the mode of the laser (continuous or pulsed), application area or spot size, and laser speed or application time [16]. The laser power level can be used to control and obtain the level of desired exterior surface finish or can be adjusted to increase manufacturing speed, printing dense part interiors where surface finish is not a factor or supports which are disposable. Continuous lasers are typically used but pulsed lasers have been used to prevent cracking during the manufacturing process. The laser spot size and speed are

critical controllable process parameters that impact how long the laser is applied to any given spot on the build plate, the size of the melt pool, and geometry resolution [17].

Powder material properties are limited in control. Different materials are available to best fit the product being manufactured but the properties of any given material are somewhat fixed, such as thermal transport properties. Thermal transport properties can cause manufacturing issues where the waste surrounding metallic powder acts as a heatsink and depending on layer patterns can cause thermal gradients within the part. In addition, light absorption, the flow of the powder, and the uniformity of each layer can be impacted by the particle shape, surface roughness, and size distributions [16].

The powder bed properties are related to, but different from, the properties of the powder material from which it is composed. The thermal properties of the powder are dependent on the packing density. One limitation of the packing density is the particle shape and size of the powder. The packing density is also correlated to the recoat process parameters such as the type of recoater (blade or roller), recoater material (metal alloy, ceramic, or plastic), velocity, powder dosing, the thickness of the applied layer, and the pressure of which the powder is applied. Figure 3 illustrates a closer look at particle arrangement in the recoat process [16,17].

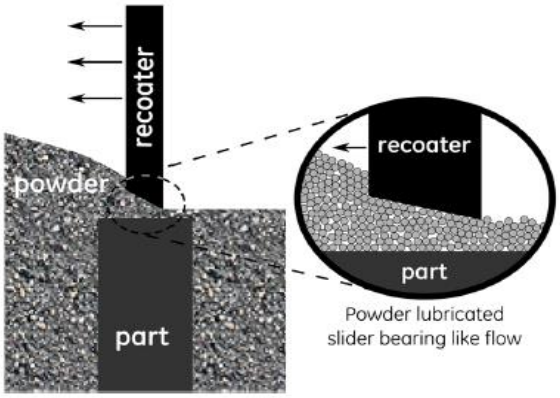

Figure 3: A closer look of particle arrangement in the recoat process [16].

The build environment has important controllable parameters. One is temperature control, which is commonly accomplished by radiant heaters or through media reservoirs, and another is the atmosphere control, such as gas content. The level of oxygen in the build atmosphere is preferred to be kept very low, preventing oxidation which could potentially impact the mechanical properties

of the finished part. This is usually controlled by the use of positive pressure inert gas (argon or nitrogen) systems and vacuum pumping from the build environment. The gas composition of the environment can also impact the surface tension and shape of the melt pool [17].

CHAPTER 2

LITERATURE REVIEW AND MOTIVATION

2.1 Overview

This chapter includes the discussion on the existing articles relevant to this study. After identifying the gap in the literature, the aims of this study have been presented.

2.2 Literature Review

Ti-6Al-4V is characterized as corrosion resistant, biocompatible, and non-toxic [19,20]. These characteristics outperformed other biomaterials to be selected for this study. Easy manufacturability of intricate structures with precise control by powder bed fusion (PBF) technology set the focal point of this study as Ti-6Al-4V cellular structures fabricated by PBF technology for cancellous bone scaffolds application. Ti-6Al-4V cellular structures combined with fabrication process would be tailored for mimicking cancellous bone mechanical properties and to be free of stress shielding effect. Researchers have explored both the electron beam and laser powered PBF technologies to manufacture Ti-6Al-4V cellular structures for cancellous bone scaffolds application [21].

Li et al. [22] successfully manufactured internal honeycomb-like cylindrical Ti-6Al-4V cellular structures using EBM. The pores of these structures were well defined, reported pore size was 1108±48μm, and completely interconnected. The compressive strength and modulus of elasticity of those structures with struts of 750±36μm in diameter and 66% porosity were 116MPa and 2.5GPa. The concluding remarks followed as these structures were strong enough for handling during implantation and somewhat comparable to the properties of human cancellous bone.

Heinl et al. [23] explored the suitability of two different cellular Ti-6Al-4V structures with a controllable interconnected porosity manufactured by EBM for bone scaffold applications. The first structure, the diamond structure, was tetrahedron in shape. The hatched structure, the second structure, was generated by maintaining parallel scanning lines with 1-mm spacing and 90° alternation of scanning directions every eight layers. This study demonstrated that the diamond structures could mimic the cancellous bone properties with the observed value of elastic modulus

(GPa), compressive strength (MPa), and porosity (%) in the range of 0.9 ±0.1-1.6 ±0.3, 21.0±0.7-29.3±0.8, and 80.8 ±0.3-81.1±0.4.

Cheng et al. [24] presented a comprehensive study on the mechanical behavior of Ti-6Al-4V stochastic foam structures and reticulated mesh structures manufactured by EBM. This study reported comparable Young's modulus and compressive strength in the range 0.2-6.3GPa and 4-113MPa, respectively, with those of trabecular and cortical bone. This study also depicted the brittle nature of these cellular structures while observing the compressive deformation behavior. The regular reticulated meshes formed crush bands at an identical angle of 45° at the time of failure whereas the stochastic foams didn't follow any specific failure modes.

Parthasarathy et al. [25] evaluated the mechanical properties of cubic Ti-6Al-4V cellular structures with porosities ranging from 49.75 to 70.32% fabricated by EBM. The reported effective stiffness and compressive strength values ranging from 0.57±0.05 to 2.92±0.17GPa and 7.28±0.93 to 163.02±11.98MPa, respectively. This study recommended that lighter structures fabricated by this technology would satisfy the functional requirements of the patient.

Marin et al. [26] observed the effects of unit cell size variation on mechanical properties for the Ti-6Al-4V cellular structures manufactured by EBM. Two-unit cells varied by unit cell surface are were explored in this study. The resulted pore size and porosity were 1400μm and 72% for the structures with bigger cells, and 650μm and 62% for the smaller cell structure. The smaller cell structures (64 MPa) were superior in compressive loading than the bigger cell structures (27 MPa).

The studies, performed by using EBM technology, indicate that the structures somewhat fell short in terms of mimicking human cancellous properties. Exploration with laser-based PBF technology shows that laser-based PBF technology is capable of manufacturing structure with better resolution and higher experimental porosity than that of EBM technology. Laser-based PBF technology alters the microstructure and eventually, alters the mechanical properties [27].

Sallica-Leva et al. [27] replicated the study performed by Parthasarathy et al. that included obtaining predefined CAD models from that study but used laser-based PBF technology instead of using EBM technology. The structures were manufactured using two different sets of energy inputs. The structures obtained from this study resulted in better dimensional accuracy and resolution. Moreover, the mechanical properties of these structures fell in the range suitable for

bone substitution applications. The compressive properties followed the predictions of the theoretical Ashby and Gibson model. Higher experimental porosities were also reported compared to those parts made by EBM technology.

Van Bael et al. [28] studied the mechanical properties Ti-6Al-4V scaffolds consisting of six different geometries with three different pore shapes (triangular, hexagonal, and square) and two different pore sizes (500 and 1000μm). These structures were manufactured by laser based PBF technology. Compression test results showed that compressive stiffness values matched the range of cortical and trabecular bone. Results from in vitro cell study, conducted to observe the cell growth behavior, recommended that a functionally graded scaffold combined with small pores would be a better choice for initial cell attachment.

Van der Stok et al. [29] studied the effectiveness of porous Ti-6Al-4V scaffolds as a biomechanically strong osteoconductive scaffold for repair of bone defects produced by laser based PBF process. Two structural variants of scaffolds were designed with nominal struts of 120μm and 230μm using a dodecahedron unit cell as a template structure and were produced in two shapes: cylindrical scaffolds for determining the compression strength and elastic modulus and femur-shaped scaffolds for determining the ultimate compression force. The reported compressive strength and elastic modulus were 14.3±1.7 MPa and 0.38±0.04 GPa for the structures with smaller nominal strut size and 77.7±12.8 MPa and 1.56±0.21 GPa for the structures with bigger strut size. However, the pore size (490μm) was bigger than the optimum pore size (250-350μm). This study indicated that structure with smaller struts is more conducive to satisfy human cancellous bone properties.

Taniguchi et al. [30] manufactured Ti-6Al-4V scaffold structures in three different pore sizes (300, 600, and 900μm) using laser-based PBF technology. The porosity was kept constant for these structures by varying the strut sizes. From the cell study, it was reported that the structure with 600μm pore size showed better bone growth capability than the other two structures for this case, especially for the joint prostheses application. The compressive strength and elastic modulus for this structure were 42MPa and 0.65GPa, respectively.

Zaharin et al. [31] investigated the mechanical properties of cubic and gyroid structures Ti-6Al-4V scaffolds with pore size ranging from 300 to 600μm fabricated by laser-based PBF technology.

It is reported that cube porous structures with pore size 0.3-0.5mm could be effective for the implant application whereas all samples of gyroid structures could be effective.

The results from these laser-based PBF studies indicated that the requirements for mimicking human cancellous bone properties have not been met yet. This necessitates the study focused on the geometry of the structure, and scanning strategies and processing parameters involved in the laser-based PBF technology. The scanning strategies and processing parameters used in L-PBF significantly impact on the surface finish and mechanical properties of the fabricated structure [32].

Heinl et al. [33] explored the effect of design variables (unit cell sizes) and processing variables (energy inputs per unit length) on mechanical properties for tetrahedron-like structures in the purpose of bone substitution applications. The linear relationship between the mechanical properties and relative density in logarithmic scale is indicated by the tests results. Using this trend, the mechanical properties can be predicted with the variation of energy input per unit length and unit cell size.

Weissmann et al. [34] investigated the mechanical properties of open-porous Ti-6Al-4V scaffolds designed in two geometrical dimensions and fabricated by laser-based PBF process. The scaffolds were twisted in design with crossing struts. This study observed the effects of the variation of processing parameters (specifically, the build orientations) with the variation of design parameters on mechanical properties. The elastic modulus of the scaffolds varied between 3.4 and 26.3 GPa due to the variation in processing parameters.

Ahmadi et al. [35] studied the effects of variation in laser power and exposure time on the properties of Ti-6Al-4V porous structures by taking a vector-based approach. The results showed that the mechanical properties were higher for higher laser power or exposure time. The reported strut sizes range from 155 to 276μm. Scaffolds with slightly better resolution struts (140 to 240μm) are reported by Wysocki et al. [36], regarded as the scaffolds having the finest struts.

These parameters studies drew the correlations between the processing parameters and mechanical properties and between the strut size variations and mechanical properties. In these cases, mechanical properties varied linearly with the increase of parameters values and strut size dimensions. However, the correlation between the scanning strategies and mechanical

properties/physical properties is still missing. This points out the necessity for a new study as the scanning strategies impact the mechanical properties of the fabricated structure significantly.

2.3 Objectives

Exploration of scanning strategies for having scaffolds with even better resolution than what has been reported in the literature and drawing a correlation between processing parameters and characteristics of scaffolds is still needed. This study is focused on the fabrication of fine-resolution Ti-6Al-4V cellular structures using laser-based PBF technology for cancellous bone scaffold purpose. The objectives of this study are summarized below-

- Designing of diamond and dodecahedron shaped cellular structures in four different unit cell sizes using CAD software,
- Identification of different laser-based PBF scanning strategies and their various associated processing parameters,
- Manufacturing of cellular structures by employing these scanning strategies with the variation of processing parameters,
- Characterizing these fabricated cellular structures in terms of scaffold resolution, porosity, and mechanical properties,
- Drawing correlations between laser-based PBF processing parameters/scanning strategies and physical/mechanical properties,
- Comparing mechanical properties with human cancellous bone properties and drawing a conclusion on the suitability for BTE applications,
- Suggesting the sets of scanning strategies and their associated processing parameters for future suitable scaffolds fabrication.

CHAPTER 3

METHODOLOGY

3.1 Overview

The details of materials and methods have been discussed in this chapter. The discussion includes Ti-6Al-4V powder characterization, designing of cellular structures, manufacturing of scaffold samples, and characterization of the manufactured samples.

3.2 Materials

Powder, used in this study, were characterized in the Metal Additive Manufacturing Laboratory (University of Memphis, Memphis, TN). The inside temperature and humidity of the lab are maintained at 23±3 °C and 30±5 %, respectively. Table 1 represents the chemical composition and Figure 4 represents the morphology of the used Ti-6Al-4V powders.

Table 1: The nominal chemical composition of the Ti-6Al-4V powders.

Element	Al	V	O	N	C	H	Fe	Y	Other	Ti
Wt.%	5.5 – 6.5	3.5 – 4.5	0.13	0.05	0.08	0.015	0.25	0.005	0.4	Bal.

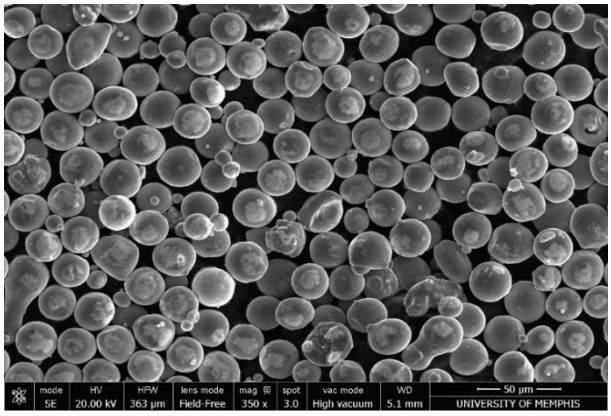

Figure 4: Morphology of the Ti-6Al-4V powders used in this study.

The size distribution, flowability, and densities of the used powders were determined by using a GilSonic UltraSiever GA-8, a Qualtech Hall Flow Meter, and a Qualtech Tap Density Meter. The powder size distributions are reported in Table 2. The range of particle size was 20-60µm, whereas

~34μm is the average size. The measured values of the apparent and tap densities were 2.41 and 2.86g/cm^3. 50g powder amount showed the flowability of 24.14s.

Table 2: Physical characterizations of the used Ti-6Al-4V powders.

Apparent Density	2.41(g/cm^3)
Tap Density	2.86 (g/cm^3)
Hall Flowability	24.14 (s/50g)
Particle Size (μm)	Weight (g/100g)
>60	0.25
≤60>53	1.85
≤53>45	10.92
≤45>38	34.42
≤38>32	29.05
≤32>25	13.56
≤25>20	5.77
≤20	3.57
Total Recovered	99.39
Average Size*	33.49±4.40

Bruker G-8 Galileo was used for measuring the Oxygen (O), Nitrogen (N), and Hydrogen (H) content of the powders whereas Bruker G-4 Icarus was used for measuring Carbon (C) content. All measurements were repeated three times and standard deviation determined. Table 3 presents the ONH and C content of the used powders. The values are slightly different than what is reported in Table 1, air and container contamination could be the reason.

Table 3: ONH-C elemental contents in the used Ti-6Al-4V powders.

Element	Used
O	1634±76 (ppm)
N	168 ±17 (ppm)
H	30±3 (ppm)
C	78±9 (ppm)

3.3 Laser-based PBF Process

Two distinct shaped unit cells, diamond and dodecahedron, were selected to be fabricated for accomplishing this study. These are the most widely explored cellular structures for bone scaffolds applications [21]. Materialise 3-Matic software (Leuven, Belgium) was used to design the base unit cells for all the cellular structures. Both diamond and dodecahedron structure were designed in four different unit cell sizes, presented in Table 4, so in total 8 structures, illustrated in Figure 5. For the diamond unit cell, the repetition of unit cells along with the in-plane directions and at the build direction was 10 and 20 times. On the other hand, for dodecahedron unit cell, the repetition of unit cells along with the in-plane directions and at the build direction was 7 and 14 times, respectively. The nominal strut sizes were considered as one of the DMLS processing parameters because they significantly influence the thermal history of the cross-section as it will be explained later. The STL files of those structures designed by Materialise 3-Matic software were transferred to Materialise Magics software. Reduction of the file size and necessary corrections were made using the Materialise Magics software. After sufficient corrections, these files were transferred to the EOSPRINT 2 software (e-Manufacturing Solutions, Germany) for defining the laser-based PBF scan strategy.

Table 4: The sizes of the unit cells for the diamond and dodecahedron structures.

Symbol	Unit cell size (mm)	
	Diamond	Dodecahedron
a_1	0.53	0.91
a_2	0.62	1.09
a_3	0.74	1.28
a_4	0.85	1.46

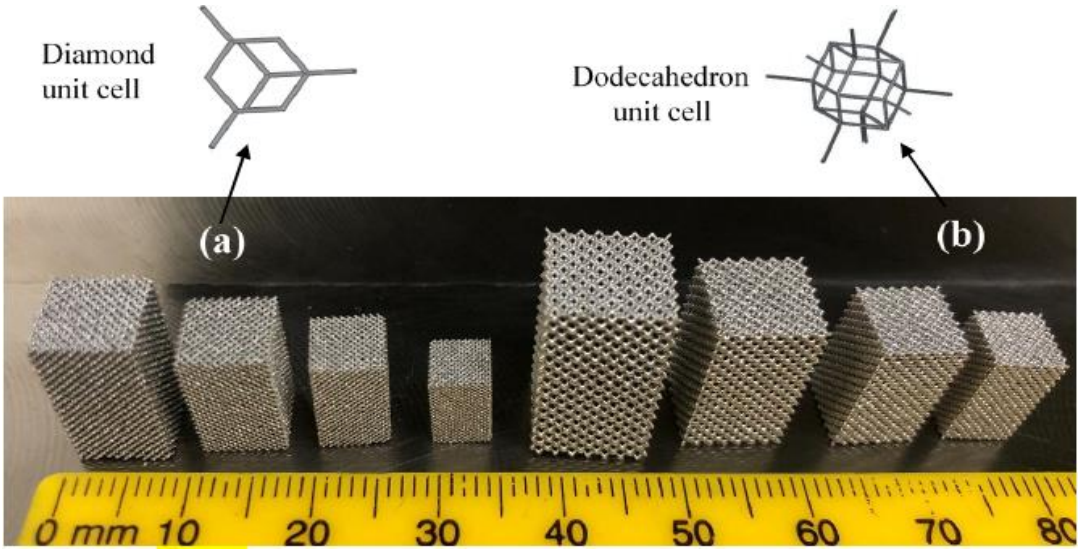

Figure 5: Eight laser-based PBF cellular structures studied herein with a) diamond unit cells and b) dodecahedron unit cells.

An EOS M290 machine was used to manufacture the cellular structures. The manufacturing build environment was argon inert. The variables remain unchanged throughout the manufacturing process were laser spot size- ~80µm, layer thickness- 30µm, laser scanning speed- 1250mm/s, build platform temperature- 37 °C, recoating speed- 150mm/s, and differential pressure- 0.6mbar. Keeping those variables fixed, three sets of scanning strategy were employed for manufacturing the structures, explained in Figure 6. For scanning strategy A, laser spot travels along a line through the center of the cross-section of the struts. A gap of 4µm was kept between the length of the line and the strut size. The starting and ending positions were offset by approximately 2µm from the strut boundary. Scanning strategy A is subcategorized into two processes- A1 and A2- by varying the laser power, 90W for A1, and 100W for A2, this allows to investigate the effect of laser powers on the properties of the cellular structures. Additionally, for scanning strategy A, other three different laser powers of 60, 70, and 80W were also used to fabricate the structures. However, lack of fusion leads to the failure of more than two structures, thus compelled to refrain from reporting. The pattern of failure was a large structure to small. It concluded that for large overhangs, the intensity of laser power should be high for scanning strategy A. The designed struts sizes for the structures fabricated by scanning strategy A are 25, 30, 35, and 40µm, denoted by a_i, where i = 1, 2, 3, and 4.

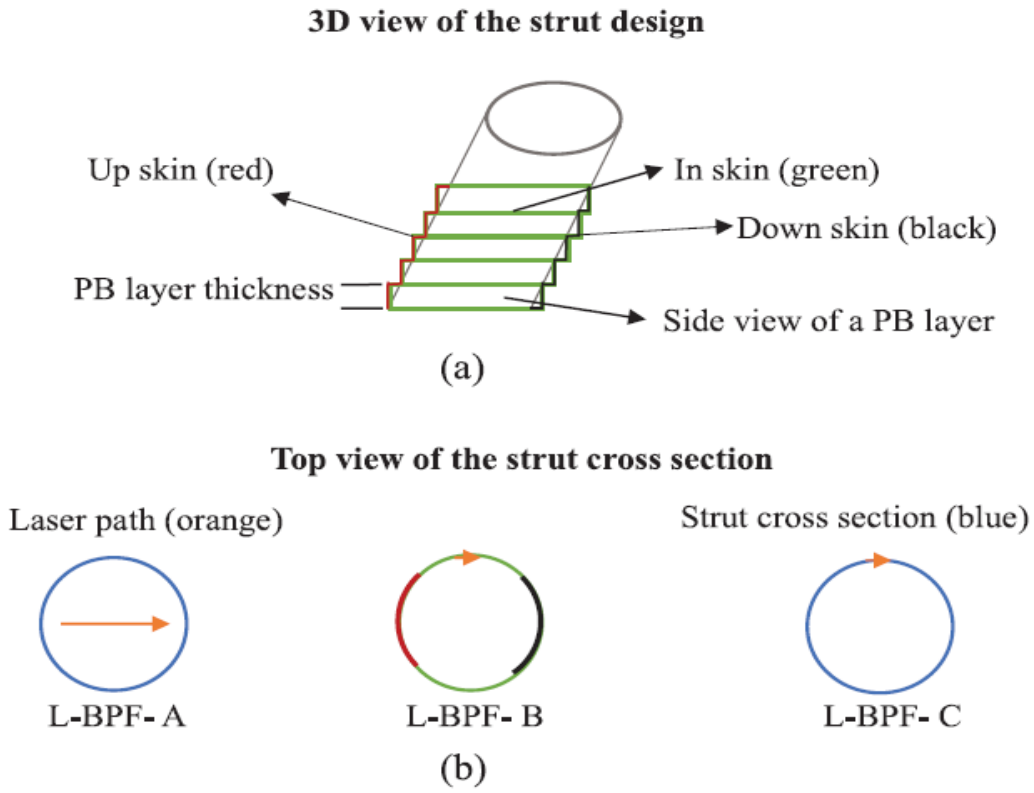

Figure 6: Illustration of the three L-PBF scan strategies used in this study: (a) 3D view and (b) top view of a strut.

Table 5: The list of processing parameters for the different scanning strategies used in this study.

Process	P (W)	d_1 (μm)	g (μm)
DMLS-A1	100	20	5
DMLS-A2	90	20	5
DMLS-B1	150*	20	5
DMLS-C1	100	20	5
DMLS-C2	100	125	15
DMLS-C3	75	125	15
DMLS-C4	50	125	15
DMLS-C5	100	125	10
DMLS-C6	100	145	10
DMLS-C7	100	165	10

* The laser power for down skin is 100 W.

All scanning strategies and processing parameters are listed in Table 5 and parameter d_1 and g are defined for determining strut size, illustrated in Figure 7. Equation (1) expresses the struts sizes as-

$$d_i = d_1 + g\,(i-1) \text{ where } 1, 2, 3, \text{ and } 4, \quad (1)$$

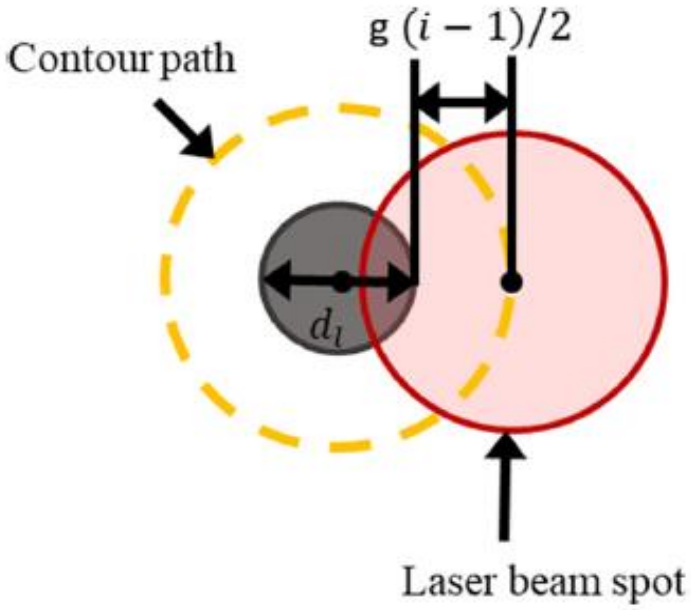

Figure 7: Illustration of the effective parameters to determine the nominal strut size.

Laser-based PBF B and C scanning strategies are defined in such a way that the laser travels along the boundary of the strut cross-sections. Scanning strategy B consists of three regions, up-skin, in-skin, and down-skin. For scanning strategy B1, laser power varies from 150W for up-skin and in-skin regions to 100W for the down-skin region. Scanning strategy C consists only down-skin region, laser power for C1 is 100W. To observe the impact of changing in scanning strategy, strut sizes for A1, B1, and C1 were kept the same.

Variations of laser powers for C2 (50W), C3 (75W), and C4 (100W) processes allow the study on the effect of change in laser power while keeping the value of parameter d1 and g constant as 125µm and 15µm, respectively. Processes C5, C6, and C7 offer the study of change in strut sizes at constant laser power (100W) and parameter g (10µm) with the variation of d1 as 125, 145, and 165µm, in order.

3.4 Geometry Measurements

After fabrication, the cellular structures were cut from the build plate using a Mitsubishi MV2400-S wire electro-discharge machine (MC Machinery Systems, INC, IL, USA). This machine uses a brass wire electrode of 0.25 mm diameter to cut the samples where distilled water acts as the dielectric fluid. Complete removal of all structures from a build plate consumed around 4 hours. A cleaning process was defined with the purpose of removing loosely attached powder. In the first step, a micro-abrasive blaster (AIR*BRASIVE® Model K, Air Abrasive Jet Technologies, LLC, NJ, USA) was used to blast the cellular structures by using 27μm aluminum oxide powder at a pressure of 85 psi, a flow rate of 0.5 CFM and a 0.018" diameter round nozzle orifice. 1-hour ultrasonic bath by using a T260-2 Zenith ultrasonic cleaner (Zenith Mfg. and Chemical Corp, USA) was the next step of the cleaning process. Later, rinsed cellular structures were dried at 100°C in a Lucifer Convection Oven (Lucifer Furnaces Inc, USA) for 30 min. At this point, blasting was repeated but this time with a flow rate of 40 g/min and air pressure of 115 psi followed a 1- hour ultrasonic bath again. The goal of this cleaning process was to remove loosely attached Ti-6Al-4V powder particles completely from the structure.

A Keyence digital microscope VHX-6000 with a capability up to 5000x magnification was used to measure the geometries of the cellular structures at 200x magnification. The strut sizes were measured at sixteen random locations for both the top and the side surfaces of the cellular structure, presented by Figure 8. Then, the averages and standard deviations of these strut sizes were reported. The intersections' height (h_d) of the struts were measured at five random locations using the same microscope. The reported heights are the height differences between the center of the strut intersections and four bordering corners.

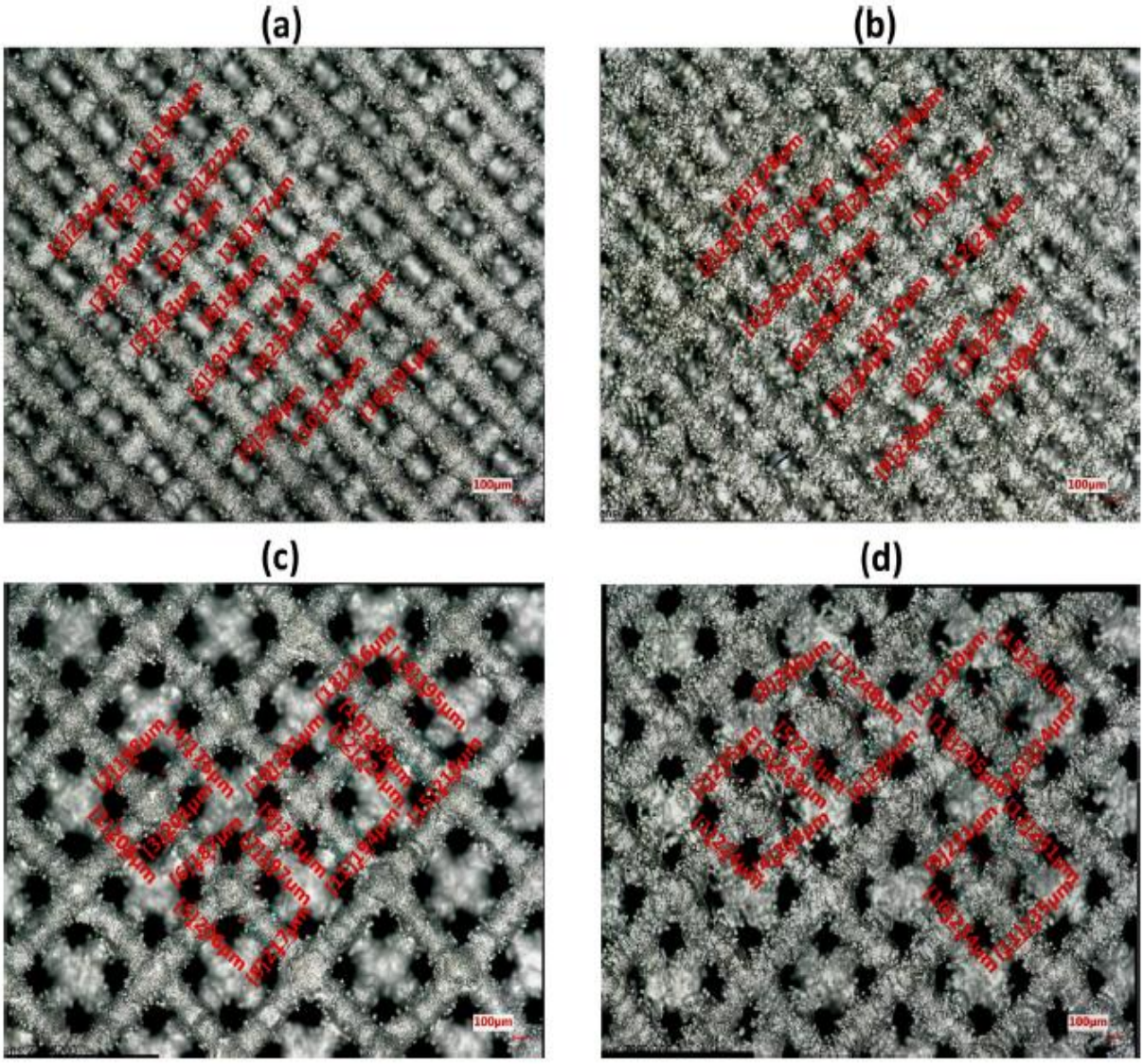

Figure 8: Illustration of the actual size measurement method used in this study: strut thickness measurements (red arrows and red font) of the diamond structure with a cell size of 0.74 mm at the (a) top surface and (b) side surface and the dodecahedron structure with a cell size of 1.27 mm at the (c) top surface and (d) side surface (magnification = 200X, scale bar = 100 μm).

3.5 Porosity

A Quantachrome Instruments Ultrpyc 1200e Pycnometer, which runs under argon gas, was used for measuring the density (ρ) of cellular structures. Density measurements were performed three times for a single sample. Moreover, the instruments ran five times per operation, allowing fifteen

measurements for each specimen, in total. This measured density was used to determine porosity, explained by equation 2-

$$\text{Porosity (\%)} = \left(1 - \frac{v_a}{v_b}\right) * 100 \quad (2)$$

Here, v_a denotes the apparent volume, calculated by dividing the mass of the structure by the density. Maas was measured by using a ME104E Mettler Toledo® scale with an accuracy of 0.0001 grams. v_b is the bulk volume of the structure, measured by an IP67 Mitutoyo digital caliper with accuracy of 0.025mm.

3.6 Mechanical Testing

A Shimadzu Autograph AGS-X universal testing machine equipped with a TRViewX digital video extensometer was used to perform the compression tests. The load cell capacity of this is 20KN. For each condition, 2-3 specimens were tested. A preload of 40N was maintained for all the tests. Tests were performed at a strain rate of 0.001s-1 (following the ISO 13314:2011 standard) and continued until the specimen failure [33]. In this study, the failure of the structure referred to the failure of the first unit cell observed by the local minimum followed by an increment in stress. The machine reported raw data as the force versus displacement (n=2 to 3) per test. Later, these data were converted to stress-strain curves using MATLAB_R2019b software.

3.7 Microhardness Testing

To perform the microhardness test, the samples were mounted using a phenolic powder in a Leco PR- 32 automatic pneumatic press. Afterward, Struers Rotoforce-4 was used to grind the samples with 220 µm and 9 µm diamond abrasive plates used along with Diapro Allergorag 9 µm size suspension for the fine grinding. Finally, the samples were polished using a colloidal silica abrasive plate of 0.04 µm size along with OP-S* (90% OP-S, 10% H_2O_2 as a suspension). Vickers microhardness tests were carried out using a Shimadzu HMV-G microhardness tester with an indentation load of 2.7 N for 10 seconds [34]. Indentations were performed by maintaining the indentation tip position right in the middle of the strut cross-sections. The microhardness measurements were conducted on eight random positions per sample and the averages and standard deviations of these measurements are reported.

3.8 Statistics

The format for reporting data is followed as the median ± standard deviation (SD). A one-way analysis of variance (ANOVA) was performed to determine the significance of the achieved results. P-values greater than 0.05 indicated the insignificant differences between the measurements. This analysis was based on two assumptions- 1) The processes consisted of a single factor and 2) all data were normally distributed.

CHAPTER 4

RESULTS

4.1 Overview

This chapter presents the direct measurements of the structure characteristics (geometry, porosity, compressive properties, and microhardness) along with the graphical representation.

4.2 Geometry Measurements

The strut size measurements both for the top and side surfaces for all the fabricated cellular structures are reported in Table 6. Similarly, Intersections height (h_d) are reported in Table 9. Table 7 and Table 8 represents the values of struts sizes from top and side along with their P-values between the processes. Both the Intersections height (hd) and strut sizes are illustrated in Figure 9. The measured sizes are different than the nominal sizes, noticeable by comparing Table 5 and Table 6. These selections aim to achieve the smallest sizes of the struts and intersections of the cellular structures that can be fabricated by laser-based PBF to mimic the lower end of the feature sizes observed in cancellous human bones. Consistent and accurate measurements of the strut sizes are challenging due to the existence of partially fused powders, can be observed from Figure 8. However, a consistent procedure was followed for all the samples to reduce the measurement errors due to the existence of the partially fused powders. The average height of the intersections shows a slight variation in a range of 40-150μm and 69-209μm for diamond and dodecahedron designs, respectively. Likewise, thicker struts were produced for dodecahedron design in all of laser-based PBF processes. The thinnest struts were observed for As scanning strategies. The little change in laser power between two As scanning strategies showed an insignificant effect on the strut thickness. The recorded thinnest strut size was 120μm, thinner than produced struts in the literature available. C4 scanning strategy also led to the thin struts because of low laser power. Due to superior energy density, the strut thickness was the highest for DMLS-B1 for both diamond and dodecahedron structures. On the other hand, the C7 scanning strategy similarly produced thick struts resulted from the growth in the nominal size of the struts. C1 and C2 strategies resulted in an insignificant variation of the manufactured strut's size though there was a sharp change in the nominal diameter from 25 to 125μm. However, increment in nominal strut size from 125 to 165μm made the struts thicker for C5 to C7 strategies.

The overall results from size measurement for two designs indicate that diamond structures experienced thinner structural features compared to dodecahedron ones. The results also imply that the cell size increase has little impact on the strut size for all of the scanning strategies.

Table 6: The measured strut sizes for the top and side surfaces of various cellular structures fabricated by the various laser-based PBF processes. The P-value indicates the significant difference between the strut sizes at the top and side surfaces.

Scanning Strategy		**Diamond**				**Dodecahedron**			
		0.53	**0.62**	**0.74**	**0.85**	**0.91**	**1.09**	**1.28**	**1.46**
A1	Top	140±25	120±16	147±22	164±21	153±31	158±18	173±35	198±19
	Side	148±20	149±17	161±24	172±24	152±19	165±23	176±35	161±24
	P-value	0.33	1e-5	0.11	0.3	0.96	0.31	0.83	0.0004
A2	Top	135±10	137±11	146±17	179±20	143±17	148±20	179±39	166±26
	Side	153±17	161±26	174±16	178±21	144±14	154±16	161±26	174±16
	P-value	0.0009	0.002	3e-5	0.8	0.88	0.35	0.99	0.43
B1	Top	213±30	230±19	207±18	216±16	243±19	243±22	247±16	237±15
	Side	264±20	270±18	292±13	241±36	272±24	288±31	270±18	292±13
	P-value	4e-6	1e-6	1e-15	0.02	0.0006	5e-5	1e-5	5e-5
C1	Top	199±18	199±17	197±13	193±12	205±17	209±12	198±21	201±11
	Side	125±25	217±15	228±10	204±16	234±22	228±16	217±15	228±10
	P-value	0.0496	0.005	2e-8	0.04	0.0002	0.0007	0.002	0.01
C2	Top	210±16	197±19	205±13	207±15	215±25	227±15	220±17	210±20
	Side	221±24	232±15	215±14	219±16	221±19	244±20	232±15	215±14
	P-value	0.12	2e-6	0.04	0.03	0.46	0.012	0.2	0.003
C3	Top	185±18	185±14	173±10	175±15	208±28	210±16	197±14	194±14
	Side	196±10	203±14	195±13	187±12	227±23	215±19	203±14	195±13
	P-value	0.03	0.0006	1e-5	0.02	0.04	0.4	0.01	0.16
C4	Top	160±16	152±15	151±17	147±17	184±18	169±17	160±17	155±18
	side	174±14	155±16	155±12	154±16	181±15	168±17	155±16	155±12
	P-value	0.007	0.58	0.49	0.28	0.59	0.9	0.02	0.0003
C5	Top	208±16	200±15	211±17	204±11	215±35	219±16	232±16	222±23
	side	209±17	224±17	220±13	210±13	247±23	248±20	224±17	220±13
	P-value	0.85	0.0002	0.09	0.15	0.004	7e-5	0.37	0.2
C6	Top	228±15	233±14	213±15	229±12	235±17	234±17	240±22	240±11
	side	228±17	245±16	235±19	240±22	262±28	248±20	245±16	235±19
	P-value	0.9	0.04	0.001	0.12	0.002	0.04	0.35	0.27
C7	Top	219±26	248±19	234±19	229±25	221±24	255±13	248±11	259±21
	side	272±17	240±22	249±15	250±13	263±22	226±24	240±22	249±15
	P-value	9e-8	0.3	0.03	0.007	1e-5	0.0002	5e-7	0.02

Table 7: The measured strut sizes on the top surface of various cellular structures fabricated by various laser-based PBF processes; the P-value shows the significant difference of the strut sizes between the structures with the same unit cell size produced by two subsequent laser-based PBF processes.

	Processes	Diamond				Dodecahedron			
		0.53	0.62	0.74	0.85	0.91	1.09	1.28	1.46
Strut Size (µm)	A1	140 ± 25	120 ± 16	147 ± 22	164 ± 21	153 ± 31	158 ± 18	173 ± 35	198 ± 19
P-value	A1–2	0.46	0.002	0.8	0.04	0.27	0.16	0.67	5e-4
Strut Size (µm)	A2	135 ± 10	137 ± 11	146 ± 17	179 ± 20	143 ± 17	148 ± 20	179 ± 39	166 ± 26
P-value	A2-B1	7e-11	6e-17	9e-11	3e-6	6e-16	8e-14	3e-7	1e-10
Strut Size (µm)	B1	213 ± 30	230 ± 19	207 ± 18	216 ± 16	243 ± 19	243 ± 22	247 ± 16	237 ± 15
P-value	B1-C1	0.12	5e-5	0.08	7e-5	1e-6	5e-6	2e-8	1e-8
Strut Size (µm)	C1	199 ± 18	199 ± 17	197 ± 13	193 ± 12	205 ± 17	209 ± 12	198 ± 21	201 ± 11
P-value	C1–2	0.08	0.67	0.06	0.01	0.16	0.001	0.002	0.13
Strut Size (µm)	C2	210 ± 16	197 ± 19	205 ± 13	207 ± 15	215 ± 25	227 ± 15	220 ± 17	210 ± 20
P-value	C2–3	1e-4	0.06	1e-8	1e-6	0.44	0.005	2e-4	0.01
Strut Size (µm)	C3	185 ± 18	185 ± 14	173 ± 10	175 ± 15	208 ± 28	210 ± 16	197 ± 14	194 ± 14
P-value	C3–4	2e-4	5e-7	1e-4	4e-5	0.007	9e-8	4e-7	8e-8
Strut Size (µm)	C4	160 ± 16	152 ± 15	151 ± 17	147 ± 17	184 ± 18	169 ± 17	160 ± 17	155 ± 18
P-value	C4–5	1e-9	6e-10	9e-11	2e-12	0.003	1e-9	6e-13	1e-10
Strut Size (µm)	C5	208 ± 16	200 ± 15	211 ± 17	204 ± 11	215 ± 35	219 ± 16	232 ± 16	222 ± 23
P-value	C5–6	0.001	2e-7	0.6	8e-7	0.05	0.01	0.2	0.007
Strut Size (µm)	C6	228 ± 15	233 ± 14	213 ± 15	229 ± 12	235 ± 17	234 ± 17	240 ± 22	240 ± 11
P-value	C6–7	0.25	0.02	0.001	0.99	0.06	4e-4	0.24	0.003
	C7	219 ± 26	248 ± 19	234 ± 19	229 ± 25	221 ± 24	255 ± 13	248 ± 11	259 ± 21

Table 8: The measured strut sizes on the side surface of various cellular structures fabricated by various laser based PBF processes; the P-value shows the significant difference of the strut sizes between the structures with the same unit cell size produced by two subsequent laser based PBF processes.

	Processes	Diamond				Dodecahedron			
		0.53	0.62	0.74	0.84	0.91	1.09	1.28	1.46
Strut Size (µm)	A1	148 ± 20	149 ± 17	161 ± 24	172 ± 24	152 ± 19	165 ± 23	176 ± 35	161 ± 24
P-value	A1–2	0.43	0.14	0.08	0.52	0.16	0.12	0.83	0.4
Strut Size (µm)	A2	153 ± 17	161 ± 26	174 ± 16	178 ± 21	144 ± 14	154 ± 16	161 ± 26	174 ± 16
P-value	A2-B1	5e-17	2e-14	2e-20	1e-6	7e-18	1e-15	2e-10	2e-11
Strut Size (µm)	B1	264 ± 20	270 ± 18	292 ± 13	241 ± 36	272 ± 24	288 ± 31	270 ± 18	292 ± 13
P-value	B1-C1	9e-7	5e-10	1e-15	0.0007	7e-5	1e-7	8e-11	7e-9
Strut Size (µm)	C1	125 ± 25	217 ± 15	228 ± 10	204 ± 16	234 ± 22	228 ± 16	217 ± 15	228 ± 10
P-value	C1–2	0.45	0.007	0.005	0.01	0.08	0.02	0.09	8e-5
Strut Size (µm)	C2	221 ± 24	232 ± 15	215 ± 14	219 ± 16	221 ± 19	244 ± 20	232 ± 15	215 ± 14
P-value	C2–3	0.0005	3e-6	0.0002	5e-7	0.43	0.0003	0.02	7e-6
Strut Size (µm)	C3	196 ± 10	203 ± 14	195 ± 13	187 ± 12	227 ± 23	215 ± 19	203 ± 14	195 ± 13
P-value	C3–4	1e-5	6e-10	5e-10	4e-7	2e-7	4e-8	9e-6	0.007
Strut Size (µm)	C4	174 ± 14	155 ± 16	155 ± 12	154 ± 16	181 ± 15	168 ± 17	155 ± 16	155 ± 12
P-value	C4–5	5e-7	1e-12	6e-15	6e-12	1e-10	4e-13	5e-11	1.5e-7
Strut Size (µm)	C5	209 ± 17	224 ± 17	220 ± 13	210 ± 13	247 ± 23	248 ± 20	224 ± 17	220 ± 13
P-value	C5–6	0.003	0.002	0.015	7e-5	0.12	0.98	0.1	0.06
Strut Size (µm)	C6	228 ± 17	245 ± 16	235 ± 19	240 ± 22	262 ± 28	248 ± 20	245 ± 16	235 ± 19
P-value	C6–7	3e-8	0.5	0.037	0.12	0.95	0.009	8e-5	0.0004
	C7	272 ± 17	240 ± 22	249 ± 15	250 ± 13	263 ± 22	226 ± 24	240 ± 22	249 ± 15

Table 9: The heights of the intersections measurements (μm) at top and side for the cellular structures manufactured with various laser-based PBF processes.

Scan Strategy		Intersection Heights h_d (μm)							
		Diamond				Dodecahedron			
Size a_i (mm)		0.53	0.63	0.74	0.84	0.91	1.09	1.27	1.45
A1	Top	53±10	65±9	78±8	116±31	125±22	104±18	114±27	133±10
	Side	88±14	106±24	150±21	140±13	122±24	140±28	157±23	190±21
A2	Top	57±11	78±7	87±12	123±12	120±40	112±18	136±11	113±14
	Side	86±18	117±14	112±13	118±29	148±35	146±15	132±35	159±37
B1	Top	61±36	79±9	48±14	114±21	127±35	125±16	161±31	156±31
	Side	84±17	85±12	115±15	135±9	163±7	189±27	188±39	167±24
C1	Top	42±13	40±17	66±27	77±17	101±28	104±24	112±16	120±14
	Side	70±13	101±21	112±13	153±24	159±14	160±21	149±23	145±17
C2	Top	40±15	42±10	65±8	70±15	94±37	97±8	90±17	120±18
	Side	44±13	105±13	122±13	156±22	163±23	158±35	182±30	166±9
C3	Top	41±4	49±7	75±7	95±12	78±16	100±21	96±18	102±31
	Side	77±17	94±24	130±3	136±30	154±10	148±26	157±29	181±40
C4	Top	42±15	62±15	83±20	120±20	92±17	99±12	106±53	83±16
	Side	78±15	100±28	122±15	157±15	154±32	156±23	144±9	132±19
C5	Top	48±10	50±14	60±12	76±17	86±40	95±15	106±14	143±34
	Side	77±17	97±19	125±9	125±17	153±19	165±31	157±13	211±41
C6	Top	61±18	58±15	65±21	92±20	126±43	97±19	111±15	123±21
	Side	78±22	103±16	129±10	137±13	158±26	168±26	175±27	180±21
C7	Top	39±18	79±30	68±11	80±33	69±11	107±25	110±9	131±16
	Side	74±12	98±14	126±23	135±24	184±20	158±39	189±37	209±41

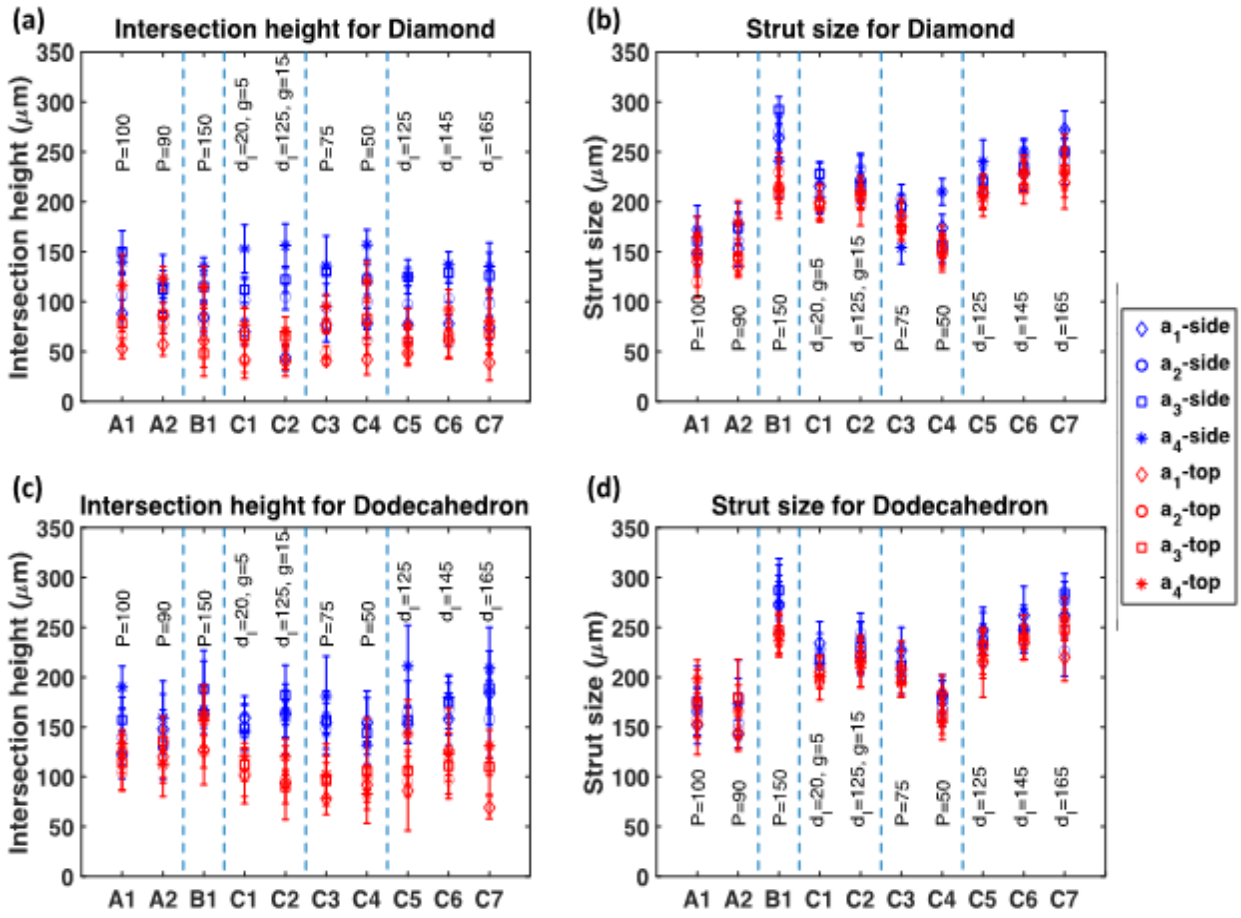

Figure 9: The intersection height and strut size for (a,b) diamond and (c,d) dodecahedron designs; the altered parameters are displayed for each laser-based PBF process.

4.3 Porosity Measurements

The density measurements were performed for two sizes of each design, showed in Table 10. The values indicated a narrow range of variation between the scanning strategies. The bulk volume of the cellular structures, measured by caliper and listed in Table 11, was used to calculate porosity using Equation 2. Porosity values are reported in Table 12 and illustrated in Figure 10. It is visible that the porosity trend is opposite to the strut size trend. Porosity increased for structures with lower strut sizes. Structures fabricated by As scanning strategies displayed higher porosity with thinner struts. Higher energy input for B1 strategy resulted in cellular structures with the lowest

porosity. The enhancement of the diameter for Cs strategies reduced the porosity of structures. Comparing the porosity in two designs, the dodecahedron structure provided higher porosity which is favorable for medical applications.

Table 10: Measured density (g/cc) of the cellular structures manufactured with various laser-based PBF processes.

	Scanning Strategies	Diamond		Dodecahedron		Solid
Unit Size (mm)	a_i	0.63	0.84	1.09	1.45	
Densities (g/cc)	A1	4.38±0.22	4.42±0.14	4.34±0.11	4.18±0.04	
	A2	4.30±0.05	4.33±0.02	4.27±0.04	4.32±0.02	
	B1	4.28±0.07	4.27±0.07	4.37±0.16	4.36±0.02	
	C1	4.33±0.03	4.40±0.06	4.46±0.08	4.36±0.08	
	C2	4.40±0.04	4.39±0.02	4.39±0.02	4.39±0.02	4.43
	C3	4.36±0.04	4.36±0.03	4.36±0.02	4.35±0.01	
	C4	4.36±0.05	4.34±0.04	4.35±0.05	4.31±0.04	
	C5	4.40±0.03	4.39±0.02	4.40±0.03	4.39±0.02	
	C6	4.35±0.08	4.32±0.18	4.39±0.05	4.37±0.05	
	C7	4.40±0.02	4.40±0.02	4.40±0.02	4.41±0.02	

Table 11: Bulk volume (cm^3) for the cellular structures manufactured with various laser based PBF processes.

Scanning Strategy	Bulk Volume (cc)							
	Diamond				Dodecahedron			
Size a_i (mm)	0.53	0.63	0.74	0.84	0.91	1.09	1.27	1.45
A1	0.243	0.428	0.679	1.029	0.458	0.785	1.239	1.873
A2	0.254	0.437	0.688	1.03	0.456	0.797	1.269	1.872
B1	0.256	0.435	0.695	1.045	0.464	0.801	1.271	1.892
C1	0.256	0.439	0.709	1.03	0.463	0.795	1.263	1.863
C2	0.256	0.441	0.697	1.03	0.47	0.808	1.277	1.891
C3	0.254	0.436	0.703	1.03	0.468	0.801	1.265	1.889
C4	0.255	0.437	0.688	1.03	0.463	0.796	1.263	1.884
C5	0.258	0.437	0.707	1.03	0.467	0.803	1.269	1.897
C6	0.26	0.445	0.705	1.06	0.472	0.809	1.285	1.942
C7	0.262	0.449	0.707	1.06	0.476	0.815	1.288	1.911

Table 12: The porosity of the fabricated laser based PBF cellular structures. The P-value indicates a significant difference in the porosity between the structures with the same unit cell size produced by two different laser-based PBF processes; e.g., P-value A1–2 refers to the P-value of the same cellular structure and with the same cell size fabricated by laser-based PBF-A1 and laser-based PBF-A2 processes.

	Processes	Diamond				Dodecahedron			
		0.53	0.62	0.74	0.85	0.91	1.09	1.28	1.46
Porosity (%)	**A1**	58.3 ± 2	68.7 ± 1.6	70.0 ± 1.0	72.6 ± 0.9	70.8 ± 0.7	77.1 ± 0.6	77.2 ± 0.2	81.3 ± 0.2
P-value	**A1–2**	0.03	0.13	0.002	3e-5	0.0008	0.0004	3e-10	2e-9
Porosity (%)	**A2**	61.8 ± 0.4	69.9 ± 0.2	71.9 ± 0.2	76.0 ± 0.1	72.6 ± 0.2	78.7 ± 0.2	81.0 ± 0.1	83.7 ± 0.1
P-value	**A2-B1**	2e-12	1e-12	1e-12	5e-12	4e-10	5e-10	5e-17	2e-16
Porosity (%)	**B1**	14.3 ± 1.5	27.7 ± 1.2	40.3 ± 1.0	54.7 ± 0.8	27.5 ± 2.8	47.0 ± 2.0	58.8 ± 0.2	69.4 ± 0.1
P-value	**B1-C1**	1e-7	8e-9	6e-10	7e-10	2e-7	4e-7	2e-10	3e-10
Porosity (%)	**C1**	30.3 ± 1.4	45.7 ± 1.1	57.7 ± 0.5	67.6 ± 0.4	48.9 ± 0.9	61.4 ± 0.7	69.4 ± 0.6	76.9 ± 0.4
P-value	**C1–2**	0.005	0.01	2e-5	7e-7	9e-17	6e-5	0.02	0.0008
Porosity (%)	**C2**	27.7 ± 0.6	43.9 ± 0.5	55.2 ± 0.2	64.8 ± 0.2	43.1 ± 0.3	59.0 ± 0.2	68.6 ± 0.1	75.9 ± 0.1
P-value	**C2–3**	1e-8	6e-10	2e-12	2e-12	2e-12	4e-12	1e-13	2e-13
Porosity (%)	**C3**	36.8 ± 0.6	53.7 ± 0.5	64.5 ± 0.2	72.2 ± 0.2	54.7 ± 0.2	66.6 ± 0.2	75.1 ± 0.1	80.6 ± 0.1
P-value	**C3–4**	2e-10	2e-10	1e-11	5e-12	3e-11	1e-11	8e-13	4e-13
Porosity (%)	**C4**	51.2 ± 0.6	64.4 ± 0.4	72.9 ± 0.3	79.2 ± 0.2	64.8 ± 0.4	74.8 ± 0.3	81.2 ± 0.2	85.7 ± 0.1
P-value	**C4–5**	4e-12	7e-13	3e-14	1e-14	4e-13	2e-13	9e-15	5e-15
Porosity (%)	**C5**	29.8 ± 0.5	43.9 ± 0.4	55.5 ± 0.2	64.0 ± 0.2	45.4 ± 0.3	59.6 ± 0.3	68.7 ± 0.1	75.3 ± 0.1
P-value	**C5–6**	0.0003	6e-6	0.0008	0.0008	2e-7	2e-7	1e-7	3e-17
Porosity (%)	**C6**	25.9 ± 1.3	38.5 ± 1.1	55.3 ± 2.2	59.9 ± 1.8	40.1 ± 0.7	55.6 ± 0.5	65.3 ± 0.4	73.0 ± 0.3
P-value	**C6–7**	0.01	0.03	0.07	0.02	5e-6	2e-6	1e-6	6e-8
Porosity (%)	**C7**	23.8 ± 0.4	37.1 ± 0.3	48.2±.0.2	57.5 ± 0.1	36.5 ± 0.3	52.6 ± 0.2	62.7 ± 0.2	70.0 ± 0.1

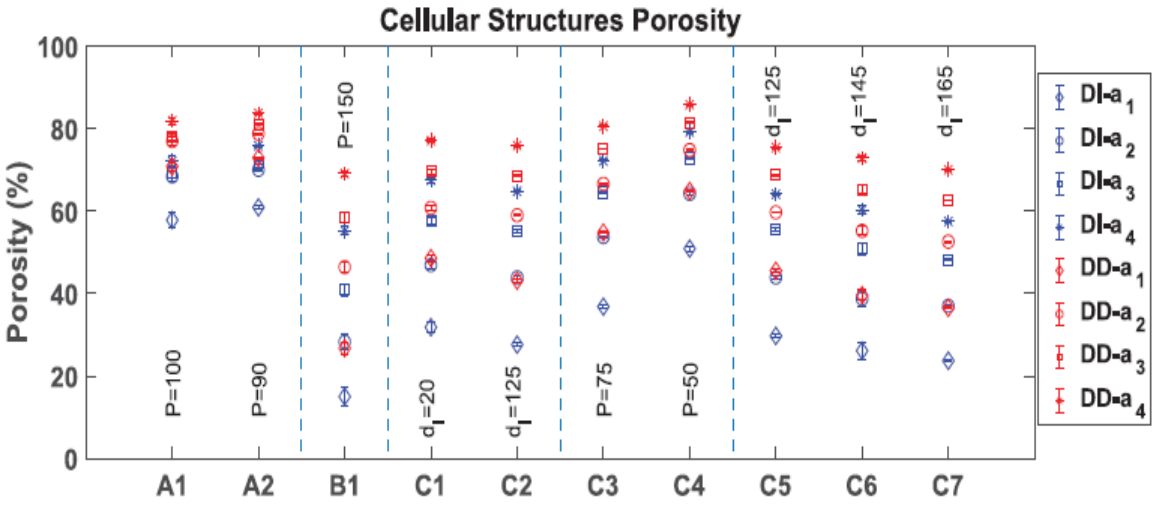

Figure 10: Porosity (%) for the cellular structures manufactured with various laser based PBF processes, where DI and DD represent the diamond and dodecahedron cellular structures, respectively.

4.4 Mechanical Properties

The mechanical properties (elastic modulus, compressive strength and % elongation) of the cellular structures are dependent on the strut sizes, presented in Table 13, Table 14, and Table 15. The values of mechanical properties are graphically presented in Figure 11 and Figure 12, and the stress-strain curves are represented by Figure 13. Scanning strategies As showed weaker properties due to higher porosity and finer struts resulted from lesser laser power. B1 produced structures with the lowest porosity and resulted in very high mechanical properties. The test for the diamond 0.53 mm size was terminated before the fracture as the value of compressive strength was too high. Scanning strategy C7 exhibits somewhat similar mechanical properties to the B1 process due to the thicker struts. The compressive strength of the structures fabricated by the rest of the Cs processes lay in between the reported compressive strength for As and B processes.

Diamond structures exhibited higher compressive strength than dodecahedron structures due to the lower porosity, indicated by . As the unit cell size increases, the enhanced porosity caused to drop in compressive strength. Moreover, dodecahedron structures, specifically with bigger unit cells, reveal higher plastic strain than diamond structures before buckling occurs. This structure exhibited more deflection under load before failure.

Table 13: Modulus of Elasticity for the dodecahedron and diamond structures with different sizes.

Scanning Strategies	Modulus of Elasticity, E (GPa)							
	Diamond				Dodecahedron			
Size ai (mm)	0.53	0.63	0.74	0.84	0.91	1.09	1.27	1.45
A1	2.6±0.1	1.8±0.0	1.6±0.0	1.6±0.0	1.5±0.1	0.8±0.1	0.7±0.0	0.5±0.0
A2	2.7±0.2	1.9±0.4	1.4±0.1	1.2±0.1	1.4±0.1	0.8±0.0	0.6±0.0	0.4±0.0
B1	7.5±0.0	5.9±0.1	4.7±0.0	3.4±0.2	5.7±0.1	4.3±0.1	3.1±0.1	2.1±0.0
C1	5.9±0.7	6.0±0.2	3.3±0.2	2.4±0.0	4.2±0.2	3.1±0.1	2.1±0.0	1.1±0.0
C2	6.5±0.2	4.7±0.2	3.6±0.0	2.7±0.1	4.6±0.1	3.4±0.2	2.1±0.1	1.3±0.1
C3	5.3±0.1	3.6±0.1	2.6±0.0	1.8±0.0	3.6±0.0	2.2±0.1	1.3±0.1	0.7±0.1
C4	3.6±0.0	2.3±0.0	1.6±0.0	0.9±0.0	2.1±0.1	1.1±0.1	0.6±0.0	0.3±0.0
C5	6.0±0.0	4.7±0.0	3.7±0.0	2.9±0.0	4.6±0.1	3.1±0.1	2.2±0.0	1.5±0.0
C6	6.2±0.3	5.0±0.3	3.9±0.1	3.0±0.3	4.8±0.5	3.5±0.2	2.6±0.1	1.8±0.1
C7	5.9±0.4	5.5±0.0	4.4±0.2	3.4±0.0	5.4±0.0	3.9±0.0	2.7±0.0	2.0±0.1

Table 14: Compressive Strength for the dodecahedron and diamond structures with different sizes.

Scanning Strategies	Compressive Strength, S (MPa)							
	Diamond				Dodecahedron			
Size ai (mm)	0.53	0.63	0.74	0.84	0.91	1.09	1.27	1.45
A1	76±10	47±1	37±1	39±1	38±4	23±2	14±2	12±2
A2	81±9	50±4	38±7	30±6	44±3	27±00	18±3	11±00
B1	>723	425±15	273±3	127±21	422±10	213±2	131±11	81±7
C1	359±42	213±9	134±12	74±8	210±11	129±7	80±6	39±1
C2	435±13	211±23	137±10	97±6	239±4	129±7	81±6	51±1
C3	265±11	139±9	85±5	55±5	164±4	92±4	52±1	26±4
C4	147±3	78±1	53±1	32±0	82±2	42±3	24±1	9±0
C5	370±0	220±12	143±4	101±5	244±9	122±3	93±2	55±8
C6	441±28	246±29	154±8	99±17	273±27	160±27	112±1	69±9
C7	488±40	333±0	205±0.1	157±0.2	347±0	192±15	120±0	83±9

Table 15: % elongation for the dodecahedron and diamond structures with different sizes.

Scanning Strategies	Elongation, δ (%)							
	Diamond				Dodecahedron			
Size ai (mm)	0.53	0.63	0.74	0.84	0.91	1.09	1.27	1.45
A1	4.1±0.7	3.6±0.0	3.2±0.2	3.4±0.0	3.9±0.3	4.0±0.5	3.0±0.5	3.2±0.3
A2	4.6±0.0	4.1±0.5	3.8±0.6	3.4±0.3	5.1±0.7	6.0±0.0	4.2±0.6	3.8±0.0
B1	>11.4	10.1±0.2	8.0±0.2	4.5±0.9	10.0±0.4	6.1±0.3	4.9±0.3	4.9±0.8
C1	7.7±0.5	6.0±0.2	5.4±0.2	3.8±0.7	6.9±0.4	6.1±0.3	6.0±0.8	5.8±0.4
C2	9.7±0.1	5.6±1.0	5.0±0.6	4.7±0.2	7.6±0.3	5.9±0.4	5.9±0.2	6.3±0.6
C3	8.1±0.8	5.5±0.6	4.7±0.4	4.1±0.5	7.7±0.4	7.2±0.3	7.9±1.0	6.7±0.1
C4	7.0±0.1	5.6±0.1	5.5±0.1	5.7±0.0	6.5±0.3	7.1±0.1	8.2±1.3	4.5±0.7
C5	8.3±0.0	6.4±1.0	5.0±0.1	4.5±0.3	8.4±0.4	5.9±0.3	6.8±0.1	6.1±1.0
C6	9.3±0.1	6.9±0.7	5.3±0.3	4.1±0.7	8.6±1.2	7.6±1.1	7.1±0.4	6.0±1.6
C7	13.2±0.9	9.32±0.0	6.41±0.4	7.09±0.3	9.44±0.0	7.5±1.4	6.8±0.0	6.8±0.7

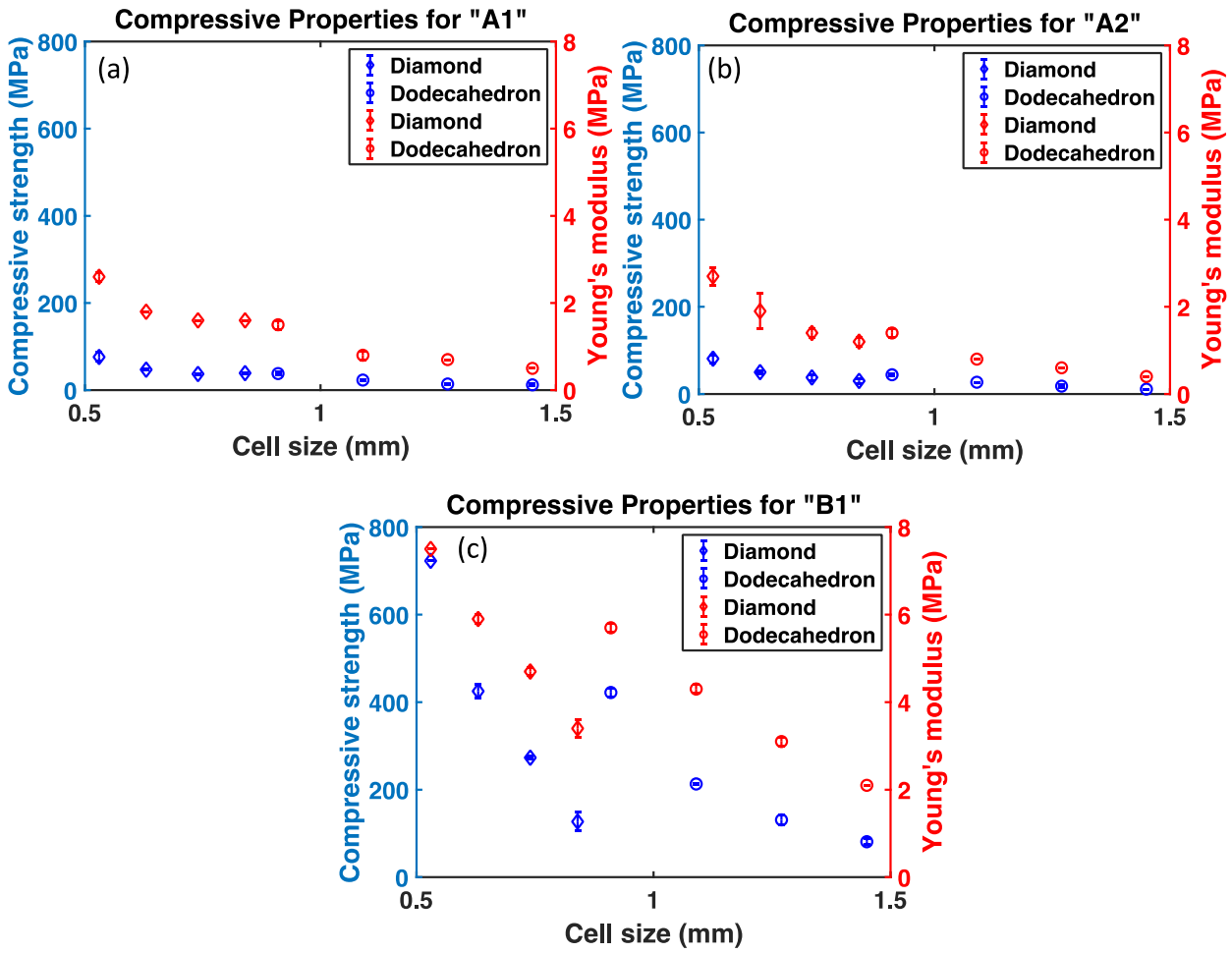

Figure 11: The variation of compressive properties versus the unit cell size for laser based PBF- (a) A1, (b) A2, (c) B1

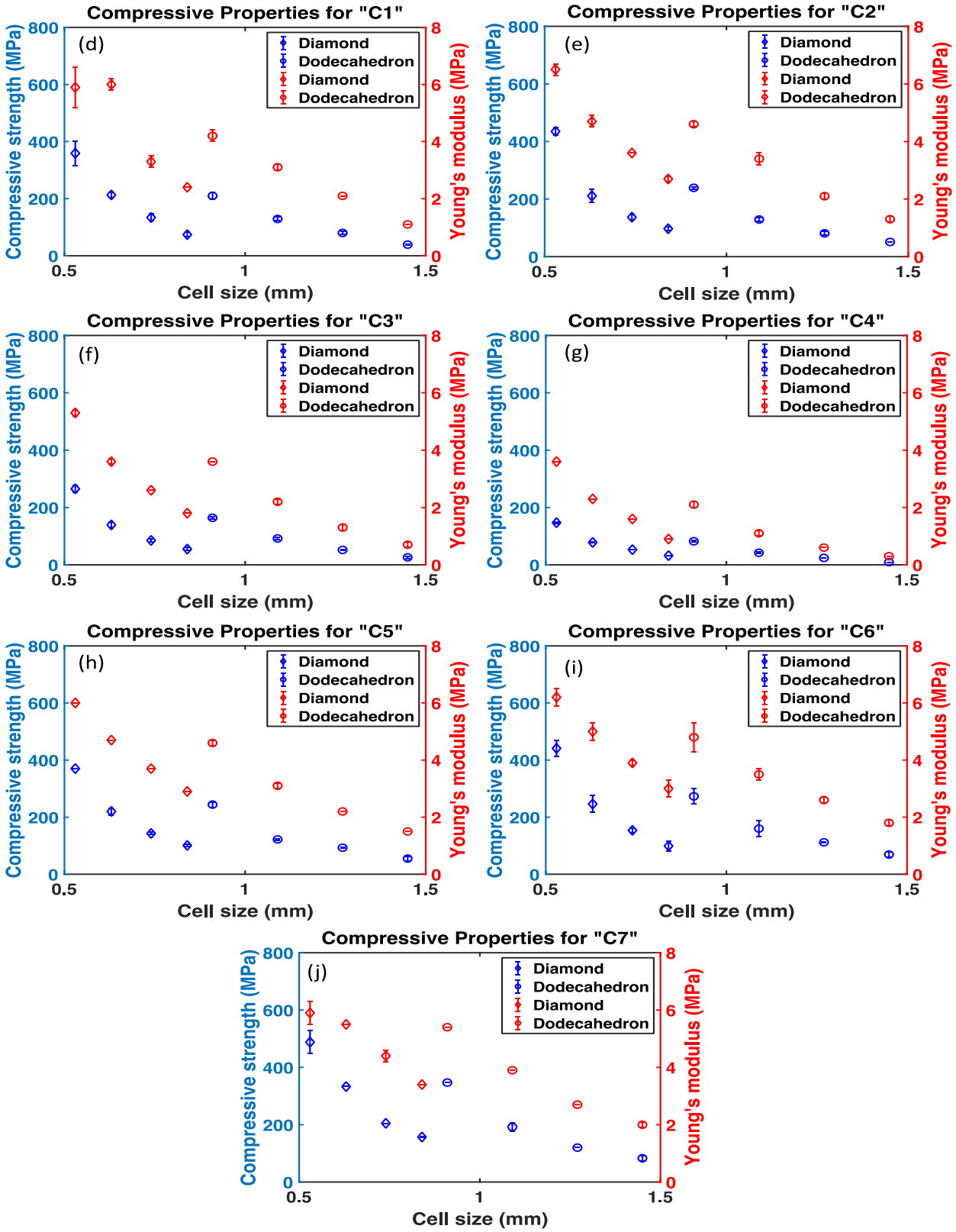

Figure 12: The variation of compressive properties versus the unit cell size for laser based PBF (d) C1, (e) C2, (f) C3, (g) C4, (h) C5, (i) C6 and (j) C7.

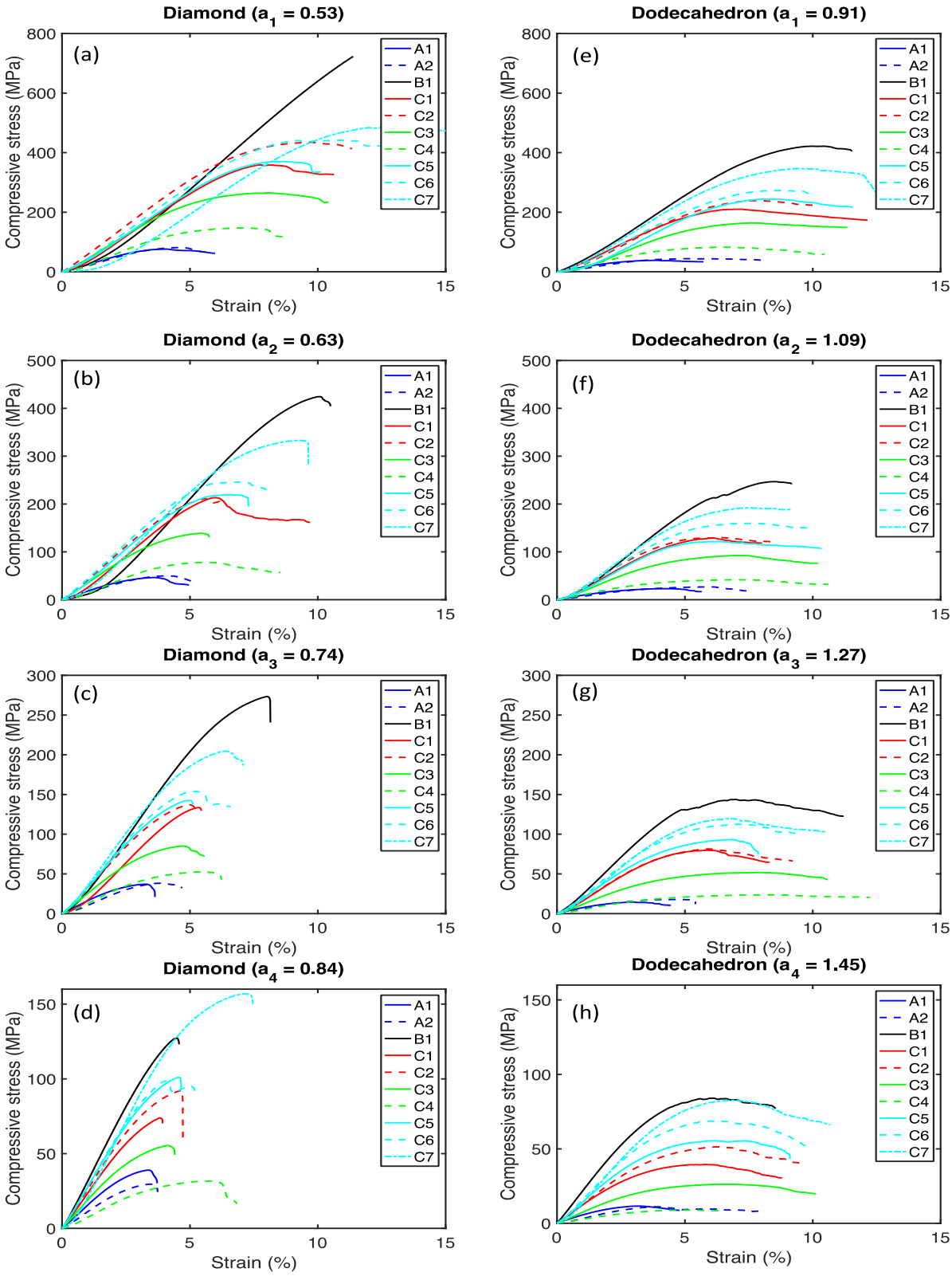

Figure 13: Compressive stresses for the dodecahedron and diamond structures with different sizes.

4.5 Microhardness

Microhardness examination was performed on the cellular structures as another mechanical property evaluation. The result of the microhardness test listed in Table 16. The indentation sizes for microhardness tests were in the range of 35-50μm, roughly about one-third compared to the finest achieved strut size (120μm). This confirmed that the border areas of the struts were avoided while testing to have acceptable hardness values. From the results, it is visible that microhardness is independent of the cell geometry and size, rather it alters with the variation of processing parameters. Then, only the samples produced by scanning strategies A1, B1, and C1 were selected to perform the test. The higher energy density of the B1 strategy resulted in a slightly higher microhardness value. No significant differences in hardness values concluded that this hardness is solely the hardness of the material itself.

Table 16: Vicker micro-hardness (HV) for the cellular structures manufactured with various laser based PBF processes.

Scanning Strategies / Design	A1	B1	C1
Diamond	336±8	357±9	347±8
Dodecahedron	337±9	361±21	349±27

CHAPTER 5

DISCUSSION

5.1 Overview

The effects of variations of geometry, processing parameters are discussed in this chapter. Moreover, the correlations between the properties and parameters are drawn here. Comparison with classical foam theory and discussion in the aspects of BTE is also presented. Lastly, the unintentional porosity contained by the structure produced in this study is discussed.

5.2 Geometry Variations for the laser based PBF Processes

Melt pool geometry caused the anisotropy in the geometry of the cellular structures. This led to the struts larger in sizes significantly ($P<0.05$) from the side surface than the top surface, indicated by Table 6. This phenomenon is applicable for all design of the cellular structures and scanning strategies. The side struts resulted from the penetration depth of the melt pool during laser-based PBF whereas sizes of the top struts were controlled by the in-plane size of the melt pool. The melt pool depth was higher than its in-plane dimensions.

As processes, where the cross-sections were scanned by a single laser track, produced the thinnest structures both for the diamond and dodecahedron design. The range of strut sizes for diamond structures were 120±16 to 172±24μm whereas for dodecahedron structures were 152±19 to 198±19μm. The strut size of 120±16μm is so far the thinnest one reported by the literature. The circular scanning path with the higher energy density of the B1 process produced significantly ($P<0.05$) thick struts both for the diamond and dodecahedron structures for both top and side compared to As processes, presented in Table 7 and Table 8. Cs processes were subjected to change in circular path radius and laser power. An increase in nominal strut size increased the thickness of struts. On the other hand, a decrease in laser power decreased the thickness of struts.

Scanning strategies with a circular scanning path produced struts with a large cross-section compared to the scanning strategies with a single laser track because of increased curing time. So, it can be described that the fine resolution of struts is the resultant of the centerline scanning strategy or low laser power of the process.

5.3 Porosity Variations with the laser based PBF Processes

The porosity of the structures was completely dependent on scanning strategies and the values were significantly ($P<0.05$) different between the processes, presented in Table 12. In addition to that, the porosity of dodecahedron structures was higher than the diamond structures. However, the difference in unit cell size could be a reason. The size of the unit cell of the dodecahedron structure was higher than the diamond unit cell.

Having the thinnest struts, the A2 process exhibited the highest porosity. In this case, porosity was in the range of 61.8±0.4 to 76.0±0.1% for diamond and in the range of 72.6±0.2 to 83.7±0.1% for the dodecahedron. Due to the centerline scanning strategy and lesser power, As strategies showed higher porosity. Similarly, the C4 process also produced structures with higher porosity. B1 process produced structures with reduced porosity because of high energy input ranging from 14.3±1.5 to 54.7±0.8% for the diamond and 27.5±2.8 to 69.4±0.1% for the dodecahedron structures. In contrast to the B1 process, C2, C3, and C4 processes consumed lesser laser power and increased the porosity of the fabricated structures significantly. However, the enhancement of nominal strut size for C5, C6, and C7 processes nullified the effect of less power and resulted in decreased porosity for the structures.

5.4 Porosity Correlations with Geometry

The structures with thick struts displayed lower porosity. The design size is an important parameter for the fabrication of cellular structures as this study indicated that the increase in the unit cell size enhanced the porosity. From the result, graphically presented in Figure 14, it is evident that the dodecahedron cellular structures fabricated by using laser-based PBF A scanning strategies with all pore sizes could mimic the porosity in cancellous bone (75-90 (%)). Slight variation in porosity for the C1 process was observed when nominal strut size varied from 20 to 35μm. This change in strut size is insignificant as the laser spot size for DMLS is 80μm, which indicates the minimum achievable size of a strut. On the other hand, the variation of nominal strut sizes from 125 to 160μm offered visible differences in porosity for the structures fabricated by Cs processes.

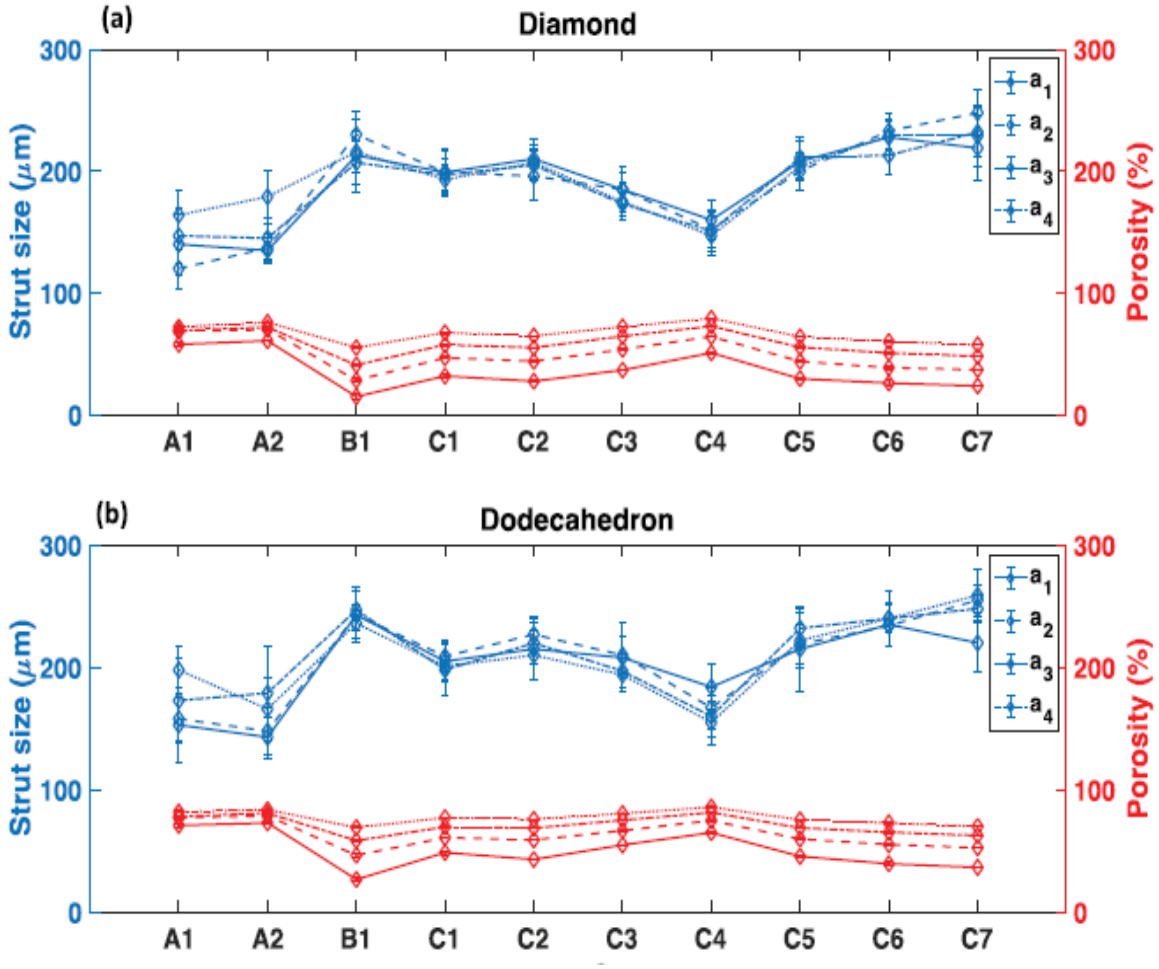

Figure 14: The variation of strut size and porosity for different laser based PBF processes.

5.5 Mechanical Property Variations as a function of the laser based PBF Processes

Cellular structures produced by the As processes were weaker than the rest of the structures. Compressive strength for the structures fabricated by the A2 process dropped from 81±9 MPa to 30±6 MPa and from 44±3 to 11±0 MPa for the dodecahedron design with the increase in unit cell size whereas the corresponding Young's modulus was in the range of 2.7±0.2 to 1.2±0.1 GPa for diamond and 1.4±0.1 to 0.4±0 GPa for dodecahedron structures. Along with A1 and A2 processes, the C4 process also produced structures with weak mechanical properties. Low laser power could be the main reason behind this phenomenon. Structures made by the B1 process exhibited superior compressive strength with the larger strut's cross-section. Similarly, with the thick struts and resultant low porosity C7 structures also showed high compressive strengths. For a few sizes of the unit cells, C7 structures were even superior in mechanical properties to B1 structures. The compressive property variations for various laser based PBF processes are shown in Figure 15.

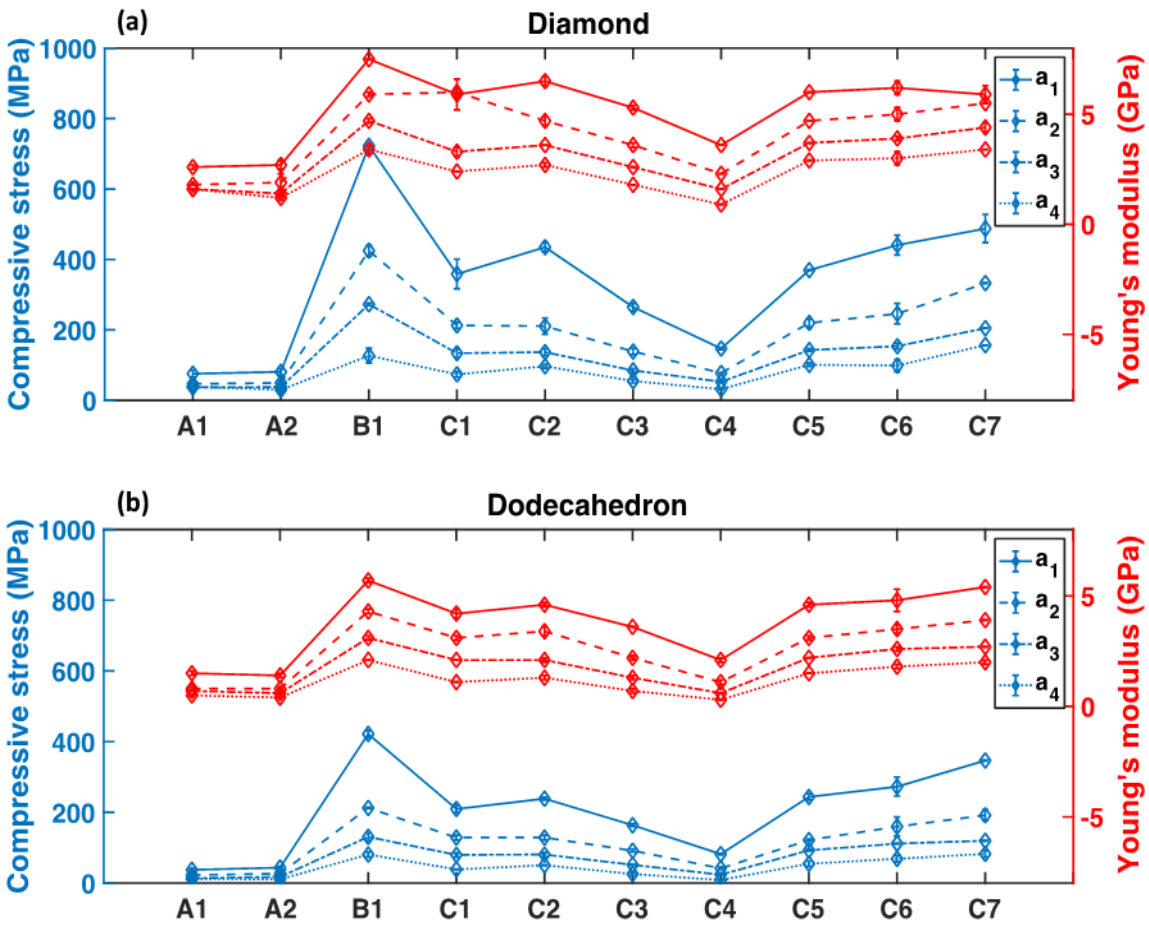

Figure 15: Compressive stress as a function of the laser based PBF processes.

5.6 Correlation between the Mechanical Properties and Porosity

The mechanical properties of the cellular structures were directly related to the porosity and strut size. The correlation can be drawn by analyzing the results of Figure 15 and Figure 16 combinedly. Basically, the larger strut's cross-section resulted in superior compressive strength in those structures. The relative density of cellular structures is supposed to be less than 0.8 to have a deviation in behavior from solid materials [35]. The material is considered as solid combined with small holes for higher relative density values. The porosity of diamond design with the small unit cell manufactured by the B1 process is 16% (relative density of 0.84) exposing the performance of solid material. The strength becomes more considerable for this structure.

5.7 Unintentional Porosity

Defects from lack of fusion and entrapped gas were prevalent in some of the structures. Lack of fusion (LOF) defects refer to the lack of fusion bonding among successive layers and hatches. LOF defects were more visible in the structures fabricated by As processes than other structures. The centerline scanning strategy could be more susceptible to LOF defects. There is no definite shape for LOFs, but elongation at the layer direction with sharp edges are common. On the other hand, the entrapped gas defects (EGD) were more common for Bs processes. High energy density to the melt pool vaporizes the powder and eventually, causes to form a gas bubble. High solidification rate does not permit these gas bubbles to escape out of the molten area. EGD is spherical or semi-spherical in nature. Both of these defects weaken the mechanical properties of the structures. Specifically, LOF enhances crack initiation under tension [37]. Unintentional porosity, presented in this study, is represented by Figure 16.

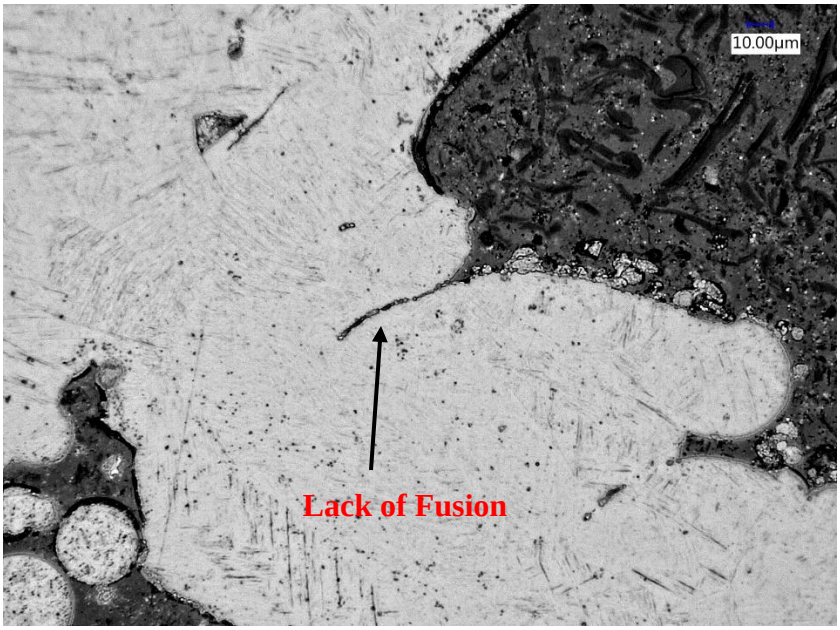

(a)

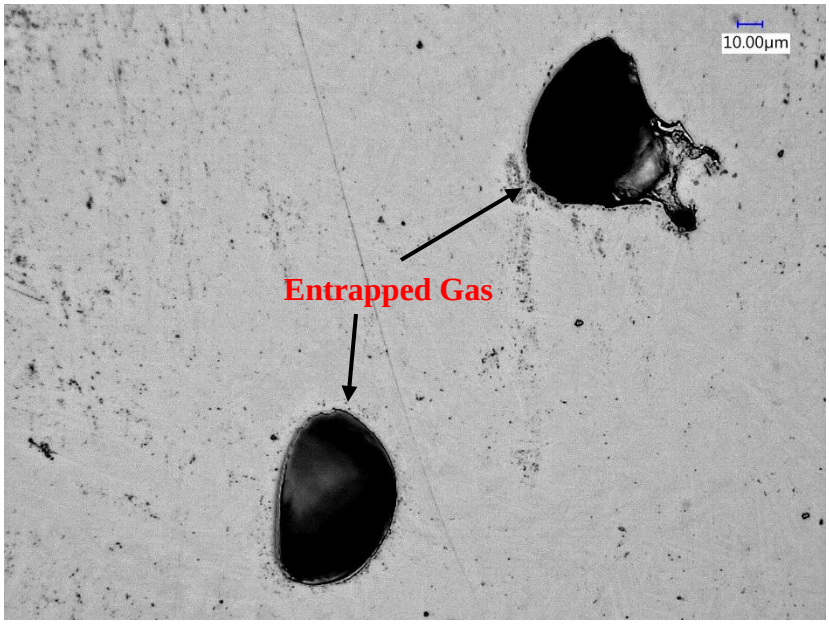

(b)

Figure 16: (a) Lack of fusion occurred in the A1 process; (b) entrapped gas in the B1 process.

5.8 Bone Tissue Engineering Discussion

To avoid the stress shielding effect, the mechanical properties of scaffolds should match with the mechanical properties of human bones. Compressive strength and elastic modulus for Cancellous tissues are in the range of 0.1-30MPa and 0.01-3GPa, in order. On the other hand, compressive strength and elastic modulus for the harder and denser (~5% porosity) cortical tissues are in the range of 130-225MPa and 3-30GPa. The porosity of cancellous bone and cortical bone is in the range of 72.6-87.4% and 2.26-5.52%, respectively [38]. In this study, the minimum porosity of the cellular structures was 15%, does not satisfy the criteria for cortical bone. Dodecahedron structures (unit cell ranged from 1.09-1.46 mm) fabricated by using As, C4, and C3 processes exhibited the properties similar to the cancellous bone properties, shown in Table 17, which could be a good fit for BTE applications. In opposition, Diamond structures with the selected unit cells would not be appropriate for BTE applications. The comparison of between the mechanical properties of cellular structures produced in this study and bone tissues is shown in Figure 17.

Table 17: Corresponding comparison of properties between Dodecahedron structures of unit cell sizes 1.09-1.45 mm and human cancellous bone.

Scanning Strategies	Dodecahedron Cell Size (mm)	Compressive Strength (MPa)	Modulus of Elasticity (GPa)	Porosity (%)
A1	1.09	23±2	0.8±0.1	77.0±1.0
	1.27	14±2	0.7±0.0	78.0±0.9
	1.46	12±2	0.5±0.0	81.9±0.8
A2	1.09	27±0	0.8±0.0	78.8±0.2
	1.27	18±3	0.6±0.0	81.0±0.2
	1.46	11±0	0.4±0.0	83.7±0.2
C4	1.09	42±3	1.1±0.1	74.8±0.3
	1.27	24±1	0.6±0.0	81.4±0.2
	1.46	9±0	0.3±0.0	85.8±0.2
Human Cancellous Bone Properties		0.1-30	0.01-3	65-90

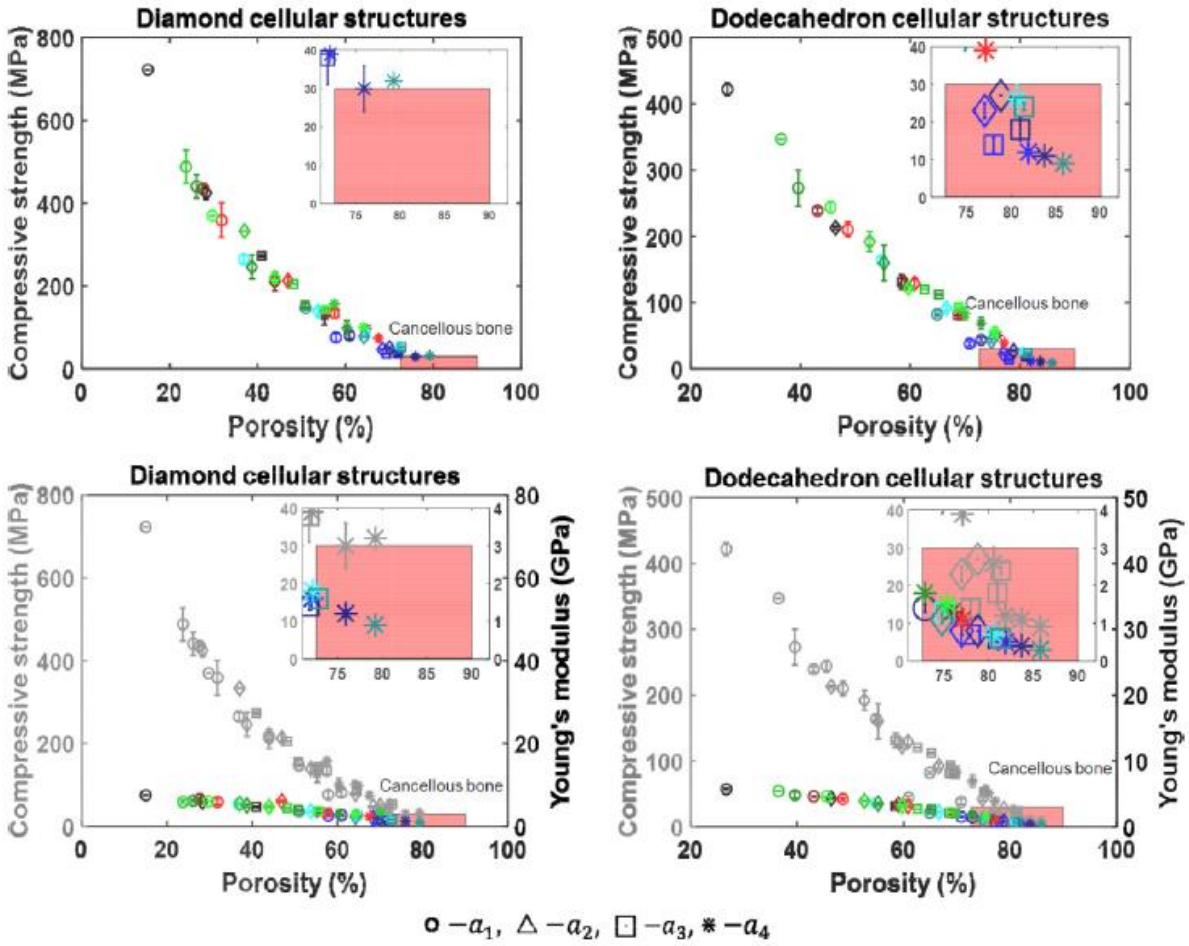

Figure 17: Comparison of properties of the cellular structures and bone tissues. Compressive strength as a function of the porosity for the (a) diamond cellular structures and (b) dodecahedron cellular structures. Young's modulus and compressive strength as a function of the porosity for the (c) diamond cellular structures and (d) dodecahedron cellular structures, where expanded views are shown in the plots.

CHAPTER 6

SUMMARY AND CONCLUSION

6.1 Summary

This study began with the demonstration of the necessity/demand for bone substitute materials which can replicate the characteristics of human bones. To understand better the underlying factors for a bone substitute material to be functional with desired properties, this study included bone biology and bone formation procedures. Similarity and necessary additional information regarding fracture healing processes than the bone formation procedures discussed subsequently. This background knowledge helped primarily to shrink the lists of bone substitute materials, specifically biomaterials, for selection in BTE purposes. An extensive study on different types of biomaterials led to shrink the lists even further and eventually, to select the materials with optimum qualities, which will facilitate bone growth at the injury site. Learning was extended to gain knowledge of different manufacturing processes to select the best fit with the given materials. In this study, the combination of materials and manufacturing processes was Ti-6Al-4V and laser-based PBF. Later, the existing literature was reviewed, and the shortcomings were identified as there is a necessity of having fine resolution scaffolds with the existing design. Before proceeding to the experiments, the structures were designed using CAD software.

Identifying the laser-based PBF scanning strategies and their associated process parameters followed by characterizing the powders were the very first steps of this study. After the determination of strategies and processing parameters, the scaffold structures were manufactured using an EOS M290 machine. The cleaning procedures were carried out to remove the loosely attached powder after the fabrication. Later, these structures were characterized in terms of porosity, mechanical properties, and physical properties. The discussion included the effects of scanning strategies and their associated parameters on the properties of the fabricated structures. This discussion extended in drawing correlations between the parameters and the properties. Lastly, the comparison between the fabricated structure properties with human bone properties drew the line of conclusion.

6.2 Conclusion

With a goal of fabricating fine resolution and light Ti-6Al-4V cellular structures for mimicking human cancellous bone for BTE, this study was focused on the investigation of laser scanning strategies and their associated processing parameters for laser based PBF processes. Three scanning strategies (categorized by centerline laser track or boundary laser track) with various combinations of processing parameters were employed to manufacture two designed cellular structure, diamond and dodecahedron, with four different unit cell sizes. The results from the evaluation of mechanical properties and geometric resolution of the fabricated cellular structures indicated that the diamond cellular structures with unit cell sizes of 0.53-0.85 mm possessed high compressive strength and Young's modulus, which cancels out the appropriateness for BTE applications. However, dodecahedron cellular structures with unit cell sizes of 1.09-1.46 mm fabricated by using the centerline laser scanning strategies or the border track scanning strategy with reduced energy density exhibited similar properties to human cancellous bone.

REFERENCES

[1] A. C. Looker, N. S. Isfahani, B. Fan, and J. A. Shepherd, "FRAX-based Estimates of 10-year probability of hip and major osteoporotic fracture among adults aged 40 and over: United States, 2013 and 2014," *Natl. Health Stat. Report.*, vol. 2017, no. 103, pp. 1–15, 2017.

[2] A. Kolk *et al.*, "Current trends and future perspectives of bone substitute materials e From space holders to innovative biomaterials," *J. Cranio-Maxillofacial Surg.*, vol. 40, no. 8, pp. 706–718, 2012, doi: 10.1016/j.jcms.2012.01.002.

[3] A. Wubneh, E. Tsekoura, C. Ayranci, and H. Uludağ, "Current State of Fabrication Technologies and Materials for Bone Tissue Engineering," *Acta Biomater.*, 2018, doi: 10.1016/j.actbio.2018.09.031.

[4] A. R. Amini, C. T. Laurencin, and S. P. Nukavarapu, "Bone tissue engineering: Recent advances and challenges," *Crit. Rev. Biomed. Eng.*, vol. 40, no. 5, pp. 363–408, 2012, doi: 10.1615/CritRevBiomedEng.v40.i5.10.

[5] C. Laurencin, Y. Khan, and S. F. El-amin, "Bone graft substitutes," pp. 49–57, 2006.

[6] S. Bose, M. Roy, and A. Bandyopadhyay, "Recent advances in bone tissue engineering scaffolds," *Trends Biotechnol.*, vol. 30, no. 10, pp. 546–554, 2012, doi: 10.1016/j.tibtech.2012.07.005.

[7] M. J. Olszta *et al.*, "Bone structure and formation: A new perspective," *Mater. Sci. Eng. R Reports*, vol. 58, no. 3–5, pp. 77–116, 2007, doi: 10.1016/j.mser.2007.05.001.

[8] C. M. Murphy, M. G. Haugh, and F. J. O'Brien, "The effect of mean pore size on cell attachment, proliferation and migration in collagen-glycosaminoglycan scaffolds for bone tissue engineering," *Biomaterials*, vol. 31, no. 3, pp. 461–466, 2010, doi: 10.1016/j.biomaterials.2009.09.063.

[9] P. Lichte, H. C. Pape, T. Pufe, P. Kobbe, and H. Fischer, "Scaffolds for bone healing: Concepts, materials and evidence," *Injury*, vol. 42, no. 6, pp. 569–573, 2011, doi: 10.1016/j.injury.2011.03.033.

[10] S. Bose, S. Vahabzadeh, and A. Bandyopadhyay, “Bone tissue engineering using 3D printing,” *Mater. Today*, vol. 16, no. 12, pp. 496–504, 2013, doi: 10.1016/j.mattod.2013.11.017.

[11] P. Chocholata, V. Kulda, and V. Babuska, “Fabrication of scaffolds for bone-tissue regeneration,” *Materials (Basel).*, vol. 12, no. 4, 2019, doi: 10.3390/ma12040568.

[12] M. A. Velasco, C. A. Narváez-Tovar, and D. A. Garzón-Alvarado, “Design, materials, and mechanobiology of biodegradable scaffolds for bone tissue engineering,” *Biomed Res. Int.*, vol. 2015, 2015, doi: 10.1155/2015/729076.

[13] G. Turnbull *et al.*, “3D bioactive composite scaffolds for bone tissue engineering,” *Bioact. Mater.*, vol. 3, no. 3, pp. 278–314, 2018, doi: 10.1016/j.bioactmat.2017.10.001.

[14] W. Jiang *et al.*, “In vitro evaluation of MgSr and MgCaSr alloys via direct culture with bone marrow derived mesenchymal stem cells,” *Acta Biomater.*, vol. 72, pp. 407–423, 2018, doi: 10.1016/j.actbio.2018.03.049.

[15] A. Eltom, G. Zhong, and A. Muhammad, “Scaffold Techniques and Designs in Tissue Engineering Functions and Purposes: A Review,” *Adv. Mater. Sci. Eng.*, vol. 2019, 2019, doi: 10.1155/2019/3429527.

[16] T. G. Spears and S. A. Gold, “In-process sensing in selective laser melting (SLM) additive manufacturing,” *Integr. Mater. Manuf. Innov.*, vol. 5, no. 1, pp. 16–40, 2016, doi: 10.1186/s40192-016-0045-4.

[17] W. J. Sames, F. A. List, S. Pannala, R. R. Dehoff, and S. S. Babu, “The metallurgy and processing science of metal additive manufacturing,” *Int. Mater. Rev.*, vol. 61, no. 5, pp. 315–360, 2016, doi: 10.1080/09506608.2015.1116649.

[18] P. K. Gokuldoss, S. Kolla, and J. Eckert, “Additive Manufacturing Processes : Selective Laser Melting , Electron Beam Melting and Binder,” 2017, doi: 10.3390/ma10060672.

[19] M. Niinomi *et al.*, “Development of low rigidity β-type titanium alloy for biomedical applications,” *Mater. Trans.*, vol. 43, no. 12, pp. 2970–2977, 2002, doi: 10.2320/matertrans.43.2970.

[20] D. McCutchen, E. Dibble, and M. M. Blount, “Phonemic effects in reading comprehension and text memory,” *Appl. Cogn. Psychol.*, vol. 8, no. 6, pp. 597–611, 1994, doi: 10.1002/acp.2350080606.

[21] X. P. Tan, Y. J. Tan, C. S. L. Chow, S. B. Tor, and W. Y. Yeong, “Metallic powder-bed based 3D printing of cellular scaffolds for orthopaedic implants: A state-of-the-art review on manufacturing, topological design, mechanical properties and biocompatibility,” *Mater. Sci. Eng. C*, vol. 76, pp. 1328–1343, 2017, doi: 10.1016/j.msec.2017.02.094.

[22] X. Li, C. Wang, W. Zhang, and Y. Li, “Fabrication and characterization of porous Ti6Al4V parts for biomedical applications using electron beam melting process,” *Mater. Lett.*, vol. 63, no. 3–4, pp. 403–405, 2009, doi: 10.1016/j.matlet.2008.10.065.

[23] P. Heinl, L. Müller, C. Körner, R. F. Singer, and F. A. Müller, “Cellular Ti-6Al-4V structures with interconnected macro porosity for bone implants fabricated by selective electron beam melting,” *Acta Biomater.*, vol. 4, no. 5, pp. 1536–1544, 2008, doi: 10.1016/j.actbio.2008.03.013.

[24] X. Y. Cheng *et al.*, “Compression deformation behavior of Ti-6Al-4V alloy with cellular structures fabricated by electron beam melting,” *J. Mech. Behav. Biomed. Mater.*, vol. 16, no. 1, pp. 153–162, 2012, doi: 10.1016/j.jmbbm.2012.10.005.

[25] J. Parthasarathy, B. Starly, and S. Raman, “A design for the additive manufacture of functionally graded porous structures with tailored mechanical properties for biomedical applications,” *J. Manuf. Process.*, vol. 13, no. 2, pp. 160–170, 2011, doi: 10.1016/j.jmapro.2011.01.004.

[26] E. Marin, S. Fusi, M. Pressacco, L. Paussa, and L. Fedrizzi, “Characterization of cellular solids in Ti6Al4V for orthopaedic implant applications: Trabecular titanium,” *J. Mech. Behav. Biomed. Mater.*, vol. 3, no. 5, pp. 373–381, 2010, doi: 10.1016/j.jmbbm.2010.02.001.

[27] E. Sallica-Leva, A. L. Jardini, and J. B. Fogagnolo, “Microstructure and mechanical behavior of porous Ti-6Al-4V parts obtained by selective laser melting,” *J. Mech. Behav. Biomed. Mater.*, vol. 26, pp. 98–108, 2013, doi: 10.1016/j.jmbbm.2013.05.011.

[28] S. Van Bael *et al.*, "The effect of pore geometry on the in vitro biological behavior of human periosteum-derived cells seeded on selective laser-melted Ti6Al4V bone scaffolds," *Acta Biomater.*, vol. 8, no. 7, pp. 2824–2834, 2012, doi: 10.1016/j.actbio.2012.04.001.

[29] J. Van Der Stok *et al.*, "Selective laser melting-produced porous titanium scaffolds regenerate bone in critical size cortical bone defects," *J. Orthop. Res.*, vol. 31, no. 5, pp. 792–799, 2013, doi: 10.1002/jor.22293.

[30] N. Taniguchi *et al.*, "Effect of pore size on bone ingrowth into porous titanium implants fabricated by additive manufacturing: An in vivo experiment," *Mater. Sci. Eng. C*, vol. 59, pp. 690–701, 2016, doi: 10.1016/j.msec.2015.10.069.

[31] H. A. Zaharin *et al.*, "Effect of unit cell type and pore size on porosity and mechanical behavior of additively manufactured Ti6Al4V scaffolds," *Materials (Basel).*, vol. 11, no. 12, 2018, doi: 10.3390/ma11122402.

[32] J. Wieding, A. Jonitz, and R. Bader, "The effect of structural design on mechanical properties and cellular response of additive manufactured titanium scaffolds," *Materials (Basel).*, vol. 5, no. 8, pp. 1336–1347, 2012, doi: 10.3390/ma5081336.

[33] P. Heinl, C. Körner, and R. F. Singer, "Selective electron beam melting of cellular titanium: Mechanical properties," *Adv. Eng. Mater.*, vol. 10, no. 9, pp. 882–888, 2008, doi: 10.1002/adem.200800137.

[34] V. Weißmann, P. Drescher, R. Bader, H. Seitz, H. Hansmann, and N. Laufer, "Comparison of single Ti6Al4V struts made using selective laser melting and electron beam melting subject to part orientation," *Metals (Basel).*, vol. 7, no. 3, 2017, doi: 10.3390/met7030091.

[35] S. M. Ahmadi, R. Hedayati, R. K. Ashok Kumar Jain, Y. Li, S. Leeflang, and A. A. Zadpoor, "Effects of laser processing parameters on the mechanical properties, topology, and microstructure of additively manufactured porous metallic biomaterials: A vector-based approach," *Mater. Des.*, vol. 134, pp. 234–243, 2017, doi: 10.1016/j.matdes.2017.08.046.

[36] B. Wysocki *et al.*, "Post processing and biological evaluation of the titanium scaffolds for bone tissue engineering," *Materials*, vol. 9, no. 3. 2016, doi: 10.3390/ma9030197.

[37] International Organization for Standardization, "Mechanical testing of metals – Ductility

testing – Compression test for porous and cellular metals (ISO Standard No. 13314:2011(E)),” *Int. Organ. Stand.*, vol. 2011, no. 1, pp. 1–7, 2011, [Online]. Available: www.iso.org.

[38] ASTM Standard, “Standard Test Method for Microindentation Hardness of Materials,” *ASTM Int.*, vol. E384, pp. 1–40, 2017, doi: 10.1520/E0384-17.

[39] E. Malekipour and H. El-mounayri, “Ehsan Malekipour & Hazim El-,” no. June, 2019, doi: 10.1007/s00170-017-1172-6.

[40] G. A. P. Renders, L. Mulder, L. J. van Ruijven, and T. M. G. J. van Eijden, “Porosity of human mandibular condylar bone,” *J. Anat.*, vol. 210, no. 3, pp. 239–248, 2007, doi: 10.1111/j.1469-7580.2007.00693.x.